Seminar Indirect

Bouke Jung, Iris de Ruiter, Paul Hofland

June 2018

Abstract

In this review we will discuss various methods to indirectly detect dark matter. Where direct detection experiments look for the scattering of a dark matter particle of nucleus of electron, indirect detection methods look for products of the annihilation of two dark matter particles. Products that we search for include gamma-rays, CMB photons, positrons, antiprotons and anti-nuclei. There have not been actual detections of the annihilation of dark matter. This non-observations give rise to strong constraints on the dark matter parameters space, ie. the dark matter mass and annihilation cross section (m_χ and $< \sigma v >$). In this review we will discuss the theoretical framework for each of these methods, the observational results and make predictions for the future.

Contents

1 Introduction - (Iris)

One of the most important questions in contemporary astrophysics is to understand the nature of dark matter in the Universe. The long-held paradigm is that dark matter is non-baryonic and cold (non-relativistic) and is made up of some Weakly Interacting Massive Particles (WIMPS). The fact that we believe dark matter is cold implies that there is a relic dark matter density from decoupling (freeze-out) of the thermal plasma in the early Universe. The most popular WIMP candidate still remains the neutralino, as predicted by the supersymmetric extension of the standard model (SUSY). For more information on the dark matter candidates see the review article about candidates on this website. Dark matter candidates are often predicted in the GeV-TeV energy range and can be detected with two distinct methods; Direct and Indirect. Note that no real dark matter signal has been detected so far (for claims of a detection see for example [1] and [2]), but certain candidates have been either constrained or excluded [3]. Despite the fact that dark matter has not been detected, indirect cosmological phenomena tell us that there must exist something like dark matter. Compelling pieces of evidence for a dark matter particle are given in the rotation curves of galaxies, the collision of the Bullet cluster and gravtiational lensing. For more information on this subject see the review about dark matter and cosmology on this website.

There are different ways to look for dark matter. Direct measurement methods looks for interactions between WIMPS and ordinary baryonic particles (such as Ge, NaI, Xe, CaF_2 molecules [4]). For more information on the direct detection of dark matter see the review article about direct detection on this website. The indirect methods looks for either gamma-rays, positrons, antiprotons and other products from dark matter annihilation. These particles are produced indirectly by pairs of WIMPs that annihilate into either quarks or leptons. Although direct $\gamma\gamma$ or $Z\gamma$ annihilation lines are in theory possible, they are loop-suppressed. Therefore, the most interesting annihilation channels are those of pairs of quarks or leptons that will further decay into gamma-rays (via for example pions), positrons and antiprotons. Uncertainty in the astrophysical background can however create issues for the latter method. To be able to distinguish for example gamma-rays from dark matter annihilation from the astrophysical background, we have to precisely know the astrophysical gamma-ray background. In this review we will discuss various methods to indirectly detect dark matter. This detection methods all look for products of the annihilation of two dark matter particles. Products that we discuss include gamma-rays, CMB photons, positrons, antiprotons and anti-nuclei. We will describe the theoretical framework for each of these methods, the observational results and make predictions for the future.

2 Gamma-ray experiments

One of the ways to indirectly detect dark matter particles is to look for the gamma-ray signature of their annihilation. Two dark matter particles can annihilate to two standard model particles which then decay and leave a distinct signature in gamma-rays. Using gamma-ray telescopes that point to different regions of the sky with different optimal energy ranges, we can probe the dark matter content within the local Universe. Gamma-rays are extremely powerful in creating a dark matter density map of the Universe since they are not deflected by magnetic fields, contrary to e.g. cosmic rays.

In section 2.1 we will discuss how the expected gamma-ray flux depends on the dark matter cross section and mass. Comparing the corresponding formulae to observations, it is possible to set an upper limit to the dark matter mass and cross section by the absence of an annihilation signal. In section 2.2 different complications in translating observation data to actual dark matter densities are discussed. Furthermore some typical examples of dark matter density profiles are explained. Finally in section 2.3 the current and future gamma-ray telescopes, and their efforts on constraining the dark matter parameters, are discussed.

2.1 Gamma-ray flux from dark matter WIMP annihilation - (Paul)

As said before, we will consider neutral WIMPs that only interact trough gravitational force and annihilate into Standard Model particles via the weak interaction. Gamma rays are one of the decay products of this annihilation. The energy and angle dependent gamma-ray brightness for this annihilation process is given by formula 1:

$$I_\gamma(E,\Theta)\& = \frac{1}{2}\frac{\langle\sigma v\rangle}{m_{DM}^2}\frac{dN_{\gamma,ann}}{dE_\gamma}\frac{1}{4\pi}\int dl\rho_{DM}^2(r[l,\Theta)) \tag{1}$$

where the first half of equation 1 depends on the particle physics model of dark matter (i.e. particle physics) and the second half on the dark matter distribution (i.e. astrophysics).

2.1.1 Particle physics factor

The velocity-averaged dark matter pair annihilation cross section $\langle\sigma v\rangle$ can be estimated by looking at the relic abundance observed today due to freeze-out and linking this to the pair annihilation rate of dark matter, which implies $\langle\sigma v\rangle \sim 3\times 10^{-26}cm^3s^{-1}$, see formula 2 [5].

$$\Omega_{DM}h^2 \sim \frac{3\times 10^{-27}cm^3s^{-1}}{\langle\sigma v\rangle} \tag{2}$$

The differential spectrum of emitted gamma-rays per annihilation, $\frac{dN_{\gamma,ann}}{dE_\gamma}$, can be seen as the sum (weighted by branching ratio, see formula 3) of all spectra final states, see figure 1. Since the branching ratio and final states are very model dependent, there are major uncertainties involved in trying to explain all observable dark matter using a single WIMP dark matter candidate. The differential spectrum is given by

$$\frac{dN_{\gamma,ann}}{dE_\gamma} = \sum_i B_i \frac{dN_{\gamma,ann}^i}{dE_\gamma} \tag{3}$$

where B_i is the model depended branching ratio, and $\frac{dN_{\gamma,ann}^i}{dE_\gamma}$ the individual final state spectra.

> shouldnt it be -26 in this eqn?

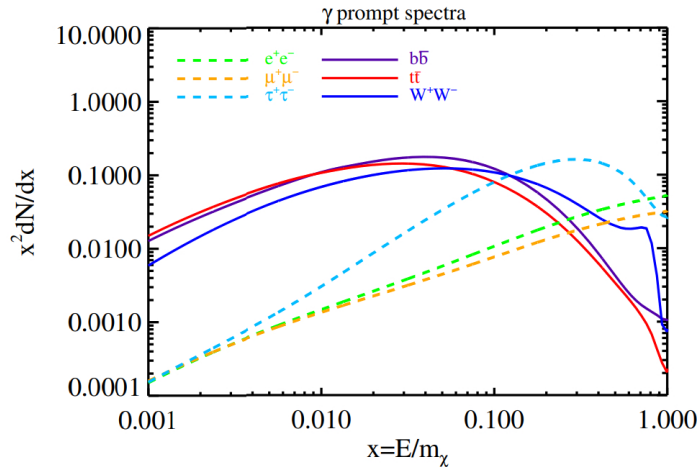Figure 1: Figure from [5]: Gamma-ray spectrum from dark matter ($m_{DM} = 500GeV$) annihilation to six different final states, calculated using PPPC4DMID [6]

The gamma-ray brightness also contains a factor $\frac{1}{2}$, which implies that dark matter is its own anti-particle, this would be a factor $\frac{1}{4}$ otherwise. And lastly dividing by m_{DM}^2 cancels out the density squared integral from the astrophysical factor.

2.1.2 Astrophysical factor

The second half of the gamma-ray brightness (formula 1), consist only of the so called J-factor, which describes the amount and distribution of dark matter in a particular source. More exact; it is the line of sight integral over the dark matter density squared (ρ_{DM}^2) at an angle from the line of sight, see formula 4 for its definition.

$$J = \frac{1}{\Delta\Omega} \int \int_{\Delta\Omega} \rho_{DM}^2(l,\Omega)dl\,d\Omega \tag{4}$$

Note that in formula 1, the factor $\frac{1}{4\pi}$ is a normalization factor that comes from integrating over solid angle.

The dark matter density functions (ρ_{DM}) are dependent on the physical situations and only depend on the radial distance to the center of the dark matter source, r. This will be explained in greater detail in chapter 2.3. To compute the line of sight integral, we first need to relate R to L and Θ (see figure 2).
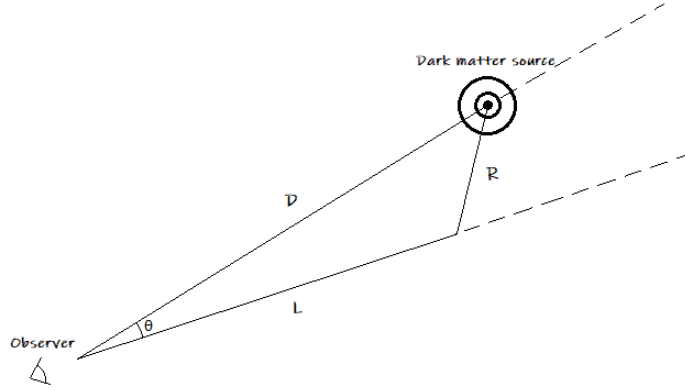
Figure 2: Top down view of observer looking down the line of sight with some angular separation Θ at a dark matter source.

Using D to denote the distance to the dark matter source and writing L for the line of sight, R for shortest distance from the line of sight to the center of the source and Θ for the angular separation of the source, we can relate R to L and Θ using the cosine rule to get formula 5.

$$R = \sqrt{L^2 + D^2 - 2L\cos\Theta} \tag{5}$$

Looking back at the total gamma-ray brightness (formula 1) and comparing this to the annihilation rate per volume, see formula 6. It becomes clear that formula 1 is just the annihilation rate per volume times the total differential spectrum of emitted gamma-rays integrated over some volume.

$$\text{Rate of annihilation per volume: } \frac{1}{2}\frac{\langle\sigma v\rangle\rho_{DM}^2}{m_{DM}^2} \tag{6}$$

2.1.3 Sagittarius gamma-ray flux

To conclude this section we show an example of a computed gamma-ray flux spectrum as a function of dark matter mass (m_χ) per annihilation channel for dwarf galaxy Sagittarius [7] (see figure 3).

Figure 3: Figure from [7]: Gamma-ray flux as a function of dark matter mass (m_χ) for different annihilation channels.

Note that the gamma-ray flux scales with $1/m_{DM}^2$, and therefore scales down exponentially with mass. In other words; higher WIMP mass means less annihilation processes per dark matter source and therefore less gamma-rays.

2.2 Probing Dark Matter Distributions - (Bouke)

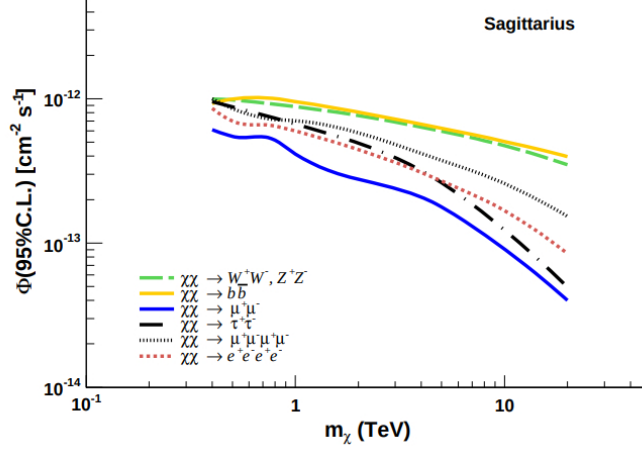Having discussed the theoretical background of indirect dark matter signals, the natural question arises how these signals actually manifest in the observable Universe. A proper answer can only be provided in the context of the distribution of dark matter within the local Universe. After all, one expects to observe a brighter gamma-ray signal in regions with high dark matter density.

Over the past decades great effort has been made to model and constrain the distribution of dark matter within the Milky Way and surrounding astrophysical objects. A few examples of recent findings are given by the discovery that the Milky Way does not conform to density profiles created from adiabatic compression [8] and the fact that neighbouring dwarf galaxies seem to exhibit dark matter distributions which become constant towards their galactic center [9]. Perhaps even more groundbreaking was the work of Diemand et al. (2008), who found evidence for the fact that dark matter can cluster together locally, forming complicated substructures which boost gamma-ray production by over an order of magnitude and cosmic ray production by a typical factor of 1.4 [10].

In this section we'll summarize some of the most prevalent models used in the context of indirect dark matter studies. Before explaining the various parameters and equations involved, however, we will first take another look at the relation between observed gamma-ray spectra and underlying dark matter distributions, in an attempt to form a better understanding of the difficulties involved with inferring flux rates from certain dark matter density profiles and vice versa.

2.2.1 Translating observational data to dark matter densities

The gamma-ray fluxes detected at observatories such as Fermi-LAT and the future CTA in principle contain all the information one needs in order to map dark matter distributions across galactic planes and large scale structures. As we've seen in section 2.1, there exists a direct theoretical correspondence between a source's gamma-ray intensity and the line-of-sight integral over the dark matter density. However, this is not the whole story. In making a direct comparison between the line-of-sight integral and observational fluxes, we implicitly neglect several processes of radiative transfer which could have

lead to redistribution of initial dark matter generated gamma-ray fluxes — not to mention the fact that some gamma-ray detections could be misinterpreted as indirect dark matter signals, having a completely different origin all the while! Hence, in order to derive accurate conclusions regarding dark matter distributions via gamma-ray fluxes, we first have to discuss radiative transfer effects. Additionally we have to exclude the possibility of misinterpreting background signals.

Once a gamma-ray has been created through dark matter annihilation or decay, several processes might occur to it which alter the gamma-ray's energy before it reaches an observatory. Most prominent are perhaps compton scattering and pair production. In the latter case, particle-antiparticle pairs (usually electrons and positrons) are formed out of two photons. A quick order-of-magnitude calculation reveals that if the dark-matter-induced gamma-ray would undergo such a process together with a typical 2.7 Kelvin photon of the comsic microwave background (CMB) (i.e. $k_B \cdot T \approx 8.6 \cdot 2.7 \approx 10^{-4} eV$) whilst traveling through the interstellar medium, it would need to have an energy of at least $E_{\gamma,1} \cdot E_{\gamma,2} \approx E_{\gamma,1} \cdot 6.6 \cdot 10^{-4} eV \approx m_e^2 \approx 2.5 \cdot 10^{11} eV^2$. Hence, the photon initially created from dark matter annihilation or decay, would be required to have an energy greater than a few hundred TeV. For space-based gamma-ray observatories such as Fermi-LAT, which generally operate at energies of a few hundred MeV to several hundred GeV, this process should therefore not constitute any impairment in detecting dark-matter-induced gamma-rays. The upcoming Cherenkov Telescope Array (CTA) which is planned to operate between a few hundred GeV and a few hundred TeV, might have to take the process into account.

Compton scattering may form a problem when the produced gamma-rays travel through areas in interstellar space with high electron densities. Typically, however, induced effects will not be very dramatic. Taking a characteristic electron density of a few particles per cubic centimetre and assuming that the Thomson approximation holds[1] we see that the optical depth associated with Compton scattering for a source at a distance of a few kpc would be:

$$\tau \approx n_e \sigma_T h d \approx 1 \, \text{cm}^{-3} \cdot 1 \times 10^{-24} \, \text{cm}^2 \cdot 1 \times 10^{22} \, \text{cm} \approx 10^{-5}$$

Hence we can conclude that galaxies are typically very optically thin when it comes to compton scattering. This allows one to largely ignore such processes in studying indirect dark matter signals, provided that the gamma-rays one observes did not have to propagate through any dense interstellar regions.

2.2.2 Dark matter distribution profiles

Provided that any ambiguities in ones signal have been thoroughly discussed and ruled out, it is in principle possible to construct dark matter density profiles for astrophysical objects using formula 2.1. Usually, however, researchers take the density profile as an input parameter and try to reproduce observed emission spectra numerically for comparison purposes. Over the years, a variety of different models have come into use [5]. The most recognizable one is perhaps the *Navarro-Frenk-White* (NFW) profile:

$$\rho_{NFW} = \frac{\rho_0}{\left(\frac{r}{r_s}\right)\left[1 + \left(\frac{r}{r_s}\right)\right]^2} \tag{7}$$

where r denotes the distance from the center of the galactic halo and r_s is a scale radius, indicatiing the point where the logarithmic derivative of the radial density profile becomes equal to -2. In the case of the Milky Way, Fornasa and Green (2014) [11] established that $r_s \approx 20$ kpc, resulting in a dark matter density at the sun's position of around $0.4 \, \text{GeV/cm}^3$ and Pato et al. (2015)

---

[1]To be precise one would need to input the Klein-Nishina cross section for this scattering process. However, since the Thomson cross section is always bigger, we can use $\sigma_T h$ instead to retrieve an upper limit.

Some slightly more involved profiles try to account for various deviations that cannot be modeled accurately by a pure NFW denisty profile. Particularly they create steeper profiles at the inner edges of the dark matter halo, since mechanisms involving (gravitational) interactions between dark matter and baryonic matter such as adiabatic contraction are expected to yield more concentrated dark matter distributions towards the galactic center [12, 13, 14]. Generalizing equation 2.2.2 and allowing for an arbitrary inner slope γ, we get the formula:

$$\rho_{GNFW} = \frac{\rho_0}{\left(\frac{r}{r_s}\right)^\gamma \left[1 + \left(\frac{r}{r_s}\right)\right]^{3-\gamma}}$$ (8)

which reverts back to equation 2.2.2 for $\gamma = 1$. Observationally, we typically find that $0 \leq \gamma \leq 1.5$, where $\gamma = 0$ corresponds to a so-called *coned* profile, whilst $\gamma = 1.5$ is also refered to as a Moore profile [15, 16].

Contrary to the above two profiles, more recent simulations seem to suggest that galactic dark matter density profiles deviate from simple power-law dependencies, displaying slopes that vary with radius instead [17, 18, 19]. One of the first attempts at modeling such irregularity was made by *Einasto* [20], who used the formula:

$$\rho_{Ein}(r) = \rho_0 \exp{-\frac{2}{a}\left[\left(\frac{r}{r_s}\right)^a - 1\right]}$$ (9)

Observations for the Milky Way yield values around 0.2 for the parameter α.

One last dark matter density profile that we'll have to discuss is provided by *the Burkert profile*:

$$\rho_{Burk}(r) = \frac{\rho_0}{\left(1 + \frac{r}{r_s}\right)\left(1 + \left(\frac{r}{r_s}\right)^2\right)}$$ (10)

This model distinguishes itself from the rest, because it quickly flattens towards the galactic core. Since many dwarf-galaxies display density profiles which strongly deviate from power-law distributions, the Burkert formula is used very frequently in the context of these objects. Considering that spheroidal dwarf galaxies generally consist of a very low density, homogeneously distributed gas, it should come as no surprise that their (dark) matter density becomes nearly constant towards the center.

Figure 4 displays the various dark matter density profiles discussed within this section in a single panel. The differences between each of the profiles is clearly visible. The GNFW profile is the steepest and leads to large densities at the galactic core. Meanwhile, the Burkert density profile quickly flattens as the radius decreases, conform our expectations for an elliptic dwarf galaxy, which generally constitute relatively low mass, and homogeneous companion galaxies to a main host.

2.3 Current and future gamma-ray telescopes and their constraints on the dark matter cross section - (Iris)

As said before we hope to detect dark matter particles via their annihilation signature. Two dark matter particles can annihilate to two standard model particles which then decay and leave a distinct signature in gamma-rays. Gamma-ray telescopes focus on the detection of gamma-rays from this dark matter annihilation process. This process is usually split up into multiple channels. The most important examples are $\chi\chi \to b\bar{b}$ and $\chi\chi \to \tau^+\tau^-$, where the free quarks and leptons will further decay into gamma-rays. The constraints given on the mass and cross section for the dark matter particle are given for each of these annihilation channels (bottom quarks and tau leptons), where the
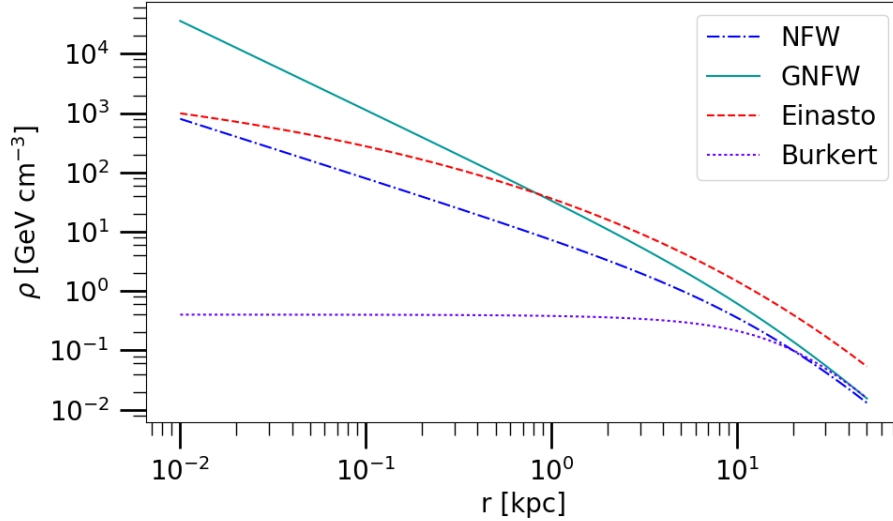
Figure 4: A graph of the various dark matter density profiles discussed within section 2.2.2. All profiles are generated using an input density $\rho_0 = 0.4$ and a scale radius $r_s = 20\,\text{kpc}$. Additionally, the GNFW spectrum was given an index $\gamma = 1.5$, whilst the Einasto spectrum received an index $a = 0.2$.

tau channel usually gives the strongest constraints. In the search for these annihilation processes most observations look directly at the dark matter halo of our Milky Way since this is one of the most dark matter dense regions (see section 2.2.1). Another way to get observations of dark matter dense regions is to observe regions around intermediate-mass black holes with masses in the range $10^2 \leq M/M_\odot \leq 10^6$, since there are enhancements (mini-spikes) of the dark matter densities around these black holes [21]. In the sections below we will discuss specific gamma-ray telescopes and their efforts in dark matter research.

2.3.1 Fermi-LAT

Most of our knowledge of gamma-ray emission from dark matter annihilation comes from the Fermi-LAT telescope. The non-detection [2] of gamma-rays from dark matter annihilation has allowed us to put strong bounds on the dark matter parameters. The LAT, which stands for Large Area Telescope, is the primary instrument on the Fermi Gamma-ray Space Telescope mission. It has a wide field-of-view for high-energy gamma-rays and it covers the range from below 20 MeV to more than 300 GeV [22]. The Fermi-LAT telescope is able to directly detect the gamma-ray emission via pair production. Observation of the Milky Way halo with Fermi-LAT provided some of the strongest constraints on the mass and cross section of the dark matter particles in the past [23].

Nowadays the best results come from the observation of dwarf spheroidal satellite galaxies (dSphs) of the Milky Way, which are some of the most dark matter dominated objects known. The lack of detection of gamma-rays gives us an upper limit to the dark matter cross section. Section 2.1 explains how the flux is related to the cross section. The newest Fermi-LAT data provide some of the most robust constraints on the dark matter mass.

For the $b\bar{b}$ annihilation channel they find $m_{DM} \gtrsim 1$ TeV and the dark matter cross section $\langle \sigma v \rangle \lesssim 1 \cdot 10^{-26} cm^3 s^{-1}$, for the $\tau\tau$ channel they find $m_{DM} \gtrsim 70$ GeV and the dark matter cross section

---

[2]Claims of gamma-ray excess have been made in the past, see for example [1] and [2], but these claims are not generally accepted as dark matter detections.

9

$\langle \sigma v \rangle \lesssim 4 \cdot 10^{-26} cm^3 s^{-1}$ [24]. The results are summarized in figure 5, where the confidence intervals in the mass - cross section plane are shown for the two annihilation channels. The solid black line shows the observed limit from the combined analysis of 15 dSphs from [25]. The dashed gray curve in this figure corresponds to the thermal relic cross section from [26]. The data points and circles in these plots represents claims of gamma-ray excesses from articles mentioned in the legend. These claims of dark matter mass and cross section can be excluded with this new data with 1σ confidence. The Fermi-LAT telescope will be able to further constrain the mass and cross section by observing the dSphs in longer observation runs and the discovery of new dSphs.
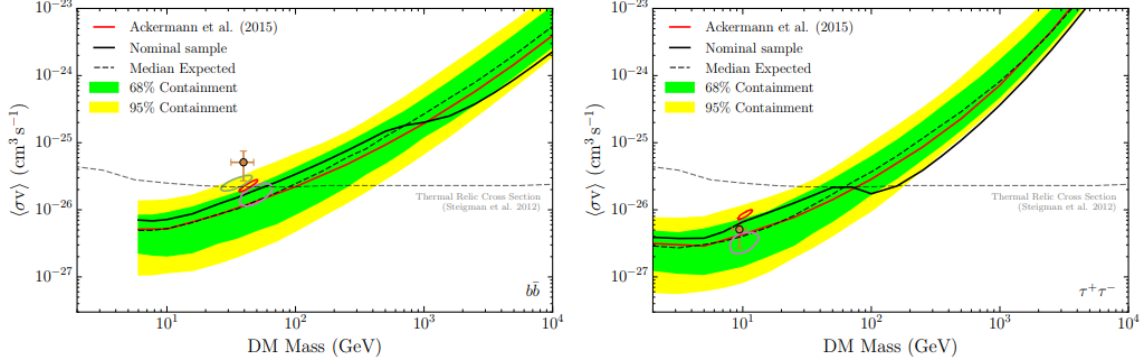

Figure 5: Figure from [24]: Constraints on the dark matter annihilation cross section at 95% CL for the $\chi\chi \to b\bar{b}$ (left) and $\chi\chi \to \tau^+\tau^-$ (right) channels derived from a combined analysis of 15 dSphs. Bands for the expected sensitivity are calculated by repeating the same analysis on 300 randomly selected sets of high-Galactic-latitude blank fields in the LAT data. The dashed line shows the median expected sensitivity while the bands represent the 68% and 95% quantiles. The solid black line shows the observed limit from the combined analysis of 15 dSphs from [25].The dashed gray curve in this figure corresponds to the thermal relic cross section from [26].

2.3.2 H.E.S.S.

Another important gamma-ray telescope is the H.E.S.S., which is an acronym for the High Energy Stereoscopic system. As opposed to the Fermi-LAT this is a ground based Imaging Atmospheric Cherenkov Telescope, which allows for much larger telescopes but also causes interference of the atmosphere with the gamma-ray detections. The H.E.S.S. collaboration shows a great evolution for constraints on the dark matter parameters over time. One of the first papers from 2006 concluded that there was no significant gamma-ray excess in the galactic center of the Milky Way [27]. In a 2011 publication they exclude cross sections larger than $\langle \sigma v \rangle = 3 \cdot 10^{-25} cm^3 s^{-1}$ for a dark matter mass of $m_{DM} \sim 1$ TeV [28]. The latest H.E.S.S. publication gives the strongest constraint on the dark matter cross section in for a $m_{DM} \sim 1$ TeV so far. The upper limit is given to be $\langle \sigma v \rangle = 4 \cdot 10^{-28} cm^3 s^{-1}$ [29].

2.3.3 VERITAS, MAGIC and HAWC

Other gamma-ray telescopes are also able to place constraints on the dark matter cross section, but these are usually less constrictive then the Fermi-LAT and the H.E.S.S. limits. VERITAS and MAGIC are both Imaging Atmospheric Cherenkov Telescope similar to H.E.S.S. but smaller in size. The HAWC is the High Altitude Water Cherenkov telescope, which uses water tanks to detect Cherenkov light from incoming gamma-rays as opposed to the atmosphere like H.E.S.S., VERITAS and MAGIC. The advantage of this technique is the ability to continuously run measurements at a wider field of

view, instead of only at night (darkness is needed of atmospheric Cherenkov imaging).

The latest VERITAS papers constrain the cross section for the bottom quark channel to $\langle\sigma v\rangle = 1.35 \cdot 10^{-23} cm^3 s^{-1}$ and for the tau lepton channel to $\langle\sigma v\rangle = 1.32 \cdot 10^{-25} cm^3 s^{-1}$ at $m_{DM} \sim 1$ TeV [30]. As said before the recent constraints from the H.E.S.S. collaboration are about 10^3 times more rigid. The MAGIC collaboration finds a strongest constraint in the tau lepton annihilation channel as well: $\langle\sigma v\rangle = 3.8 \cdot 10^{-24} cm^3 s^{-1}$ at $m_{DM} \sim 0.5$ TeV [31]. Finally there is HAWC which only started observing recently and therefore has not produced constraints nearly as strong as other telescopes yet [32].

2.3.4 Future telescopes

In the near future the Cherenkov Telescope Array (CTA) hopes to improve the current limits set by H.E.S.S [34]. The CTA experiment will be the largest Imaging Atmospheric Cherenkov Telescope, taking into account telescope arrays in the northern and southern hemisphere. Since these telescopes vary in size, the CTA will improve sensitivity over a large energy range. They will be able to constraint the dark matter cross sections for dark matter masses ranging from 100 GeV to tens of TeV, with a sensitivity improved by a factor of 5-10 [34]. Fig. 6 shows how the CTA will hope to improve the dark matter cross section over a wide energy range. The sensitivity is shown in comparison with the strongest Fermi-LAT and H.E.S.S. constraints. It is important to note that these predictions are made by the CTA consortium itself. Critics of these optimistic constraints say that the actual CTA cross section constraints will be an order of magnitude weaker than estimated by the CTA consortium [35]. Here the galactic diffuse gamma-ray emission and systematic errors that will decrease the CTA sensitivity are properly taken into account.
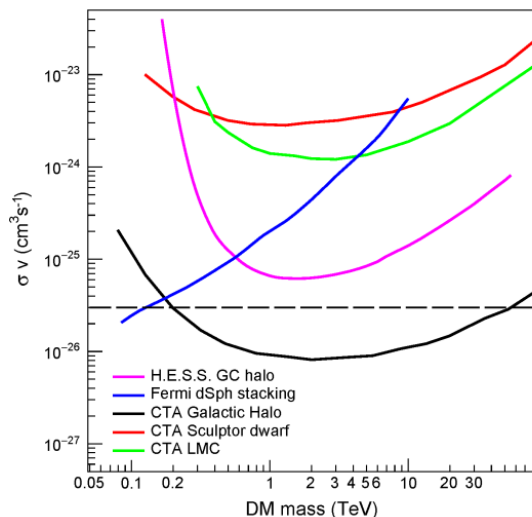
Figure 6: Figure from [33]: comparison of predicted sensitivities in for the targets of: the Milky Way Galactic halo: the Large Magellanic Cloud (LMC) and the dwarf galaxy Sculptor. The CTA sensitivity curves use the same method and W^+W^- annihilation modes for each target and the Einasto dark matter profile. The sensitivities for the three targets are all for 500 hours taking into account the statistical errors only.

Other planned gamma-ray telescope arrays include the CALET, GAMMA-400 and HERD. The first two telescopes have been launched recently and will improve the current resolution in small energy ranges [36, 37]. They will however not be able to improve the limits on the continuous spectrum, as set by Fermi-LAT. The HERD telescope is set to launch in 2020, and will be the most sensitive gamma-ray telescope in the 10 GeV to 1 TeV range [38]. At higher energies the Cherenkov telescopes will do better, since they have a larger effective area.

2.3.5 Comparison of gamma-ray telescopes

Table 1 shows a comparison of the discussed current (top) and future (bottom) gamma-ray telescopes in energy range, field of view, constraints on dark matter masses and cross sections.

11

Table 1: Comparison of different current (top) and future (bottom) gamma-ray telescopes in energy range, field of view (f.o.v.), constraints on dark matter masses and cross sections. The right column shows the references for these parameters. *: $\frac{2}{3}$ of the sky. **: these are the optimistic constraints as set by the CTA consortium. Critics thinks that the actual cross section constraints will be up to an order of magnitude higher [35]. ***:geometric factor $> 3m^2$ sr.

Name	Energy range	F.o.v ($°$)	m_{DM}	σv (cm^3/s)	Ref
Fermi-LAT	20 MeV - 300 GeV	4.2	~ 10 GeV	$\sim 4 \cdot 10^{-26}$	[22], [24]
H.E.S.S	300 GeV - 70 TeV	3.5	~ 1 TeV	$4 \cdot 10^{-28}$	[29]
Veritas	85 GeV - 30 TeV	3.5	~ 1 TeV	$2.85 \cdot 10^{-24}$	[30]
Magic	100 GeV - 100 TeV	3.5	~ 0.5 TeV	$3.8 \cdot 10^{-24}$	[31]
HAWC	500 GeV - 100 TeV	*	~ 1 TeV	$\sim 10^{-24}$	[32]
CTA	100 GeV - 10 TeV	4-5	~ 1 TeV	$5 \cdot 10^{-27} - 3 \cdot 10^{-26}$ **	[33], [34]
CALET	100 GeV - 1 TeV	45-58	—	—	[36]
GAMMA400	20 MeV - 1 TeV	60	—	—	[37]
HERD	10 GeV - 1 TeV	***	10 GeV 1 TeV	$6 \cdot 10^{-30} - 5 \cdot 10^{-29}$ $4 \cdot 10^{-27} - 9 \cdot 10^{-27}$	[38]

2.4 Smoking gun for the detection of dark matter annihilation - (Iris)

All gamma-ray measurements so-far have not detected any anomalies with respect to the background. Therefore we have only been able to put constraints on the dark matter cross section and mass. If we were able to reach sensitivity that we could actually probe the gamma-ray signal from dark matter annihilation, we could predict what this signal would look like. A smoking gun for a dark matter detection would be a spiked flux around a typical energy in a number of sources (for example multiple dwarf galaxies). Such a spiked flux usually lies at twice the annihilating particle's mass. So if such a flux spike would be observed in multiple sources at an energy that is not compatible with any other standard model particle, we would have build have very strong case for a dark matter detection.

3 CMB constraints on dark matter

Another way to possibly detect dark matter is via its imprint on the Cosmic Microwave Background (CMB). Around the time of recombination ($z \sim 1000$) the secondary particles of dark matter annihilation would have affected other processes and therefore would have left an imprint on the CMB [39]. One of the biggest achievements of modern cosmology is the remarkable agreement between the theoretical description of recombination and the observations of the CMB. Our standard model of recombination is severely constrained by the CMB data, ie. changing the recombination model while staying in agreement with the CMB data has proven difficult [40]. Examples of refinements to the current recombination model are delayed recombination [41] and accelerated recombination [42], both of which turned out to correspond badly with the available CMB data. Measurements of the CMB by WMAP and more recently by Planck are able to put constraints on dark matter models.

3.1 Cosmological history with the CMB power spectrum - (Iris)

Figure 7 shows the theoretical CMB power spectrum, compared to the most recent Planck data [43]. As said before, one of the greatest achievements of modern cosmology is the remarkable agreement between our current ΛCDM model (red) and data (blue). We can even use this agreement to constrain the dark matter cross section. To do so it is important to fully understand the (bumps in the) CMB power spectrum and how they are affected by altering the theoretical input.
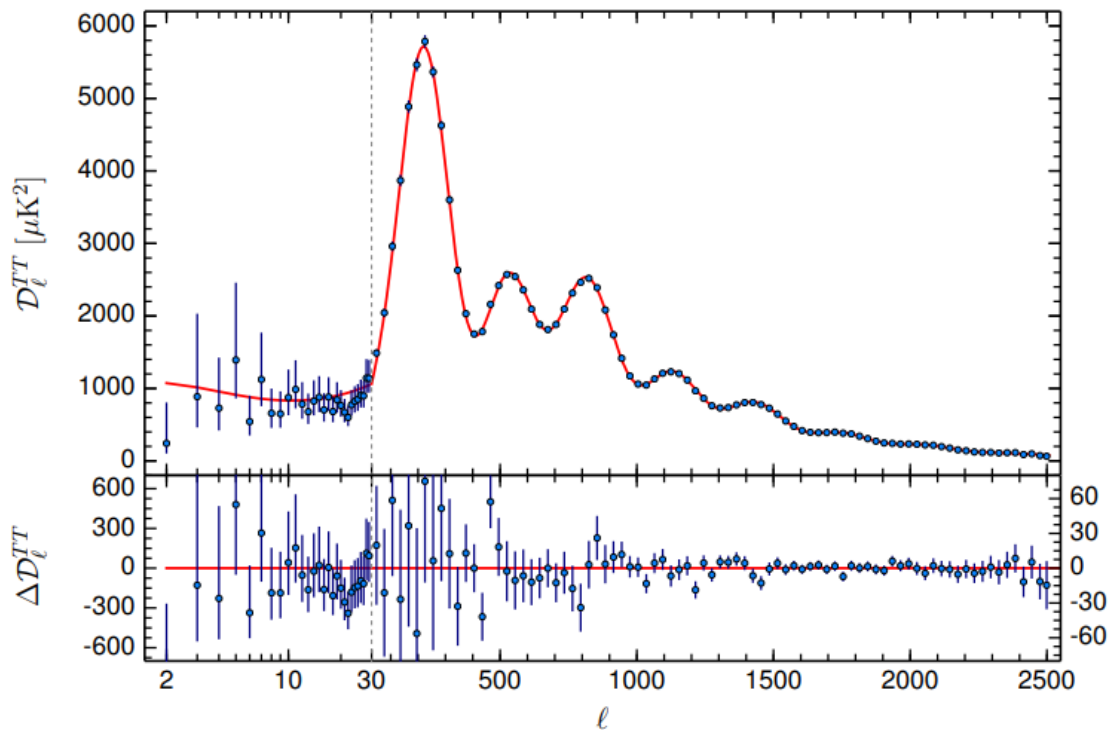

Figure 7: Planck 2015 CMB spectra, compared with the base ΛCDM fit to Planck data (red line). The upper panel show the spectra and the lower panel shows the residual. The horizontal scale changes from logarithmic to linear at the "hybridization" scale, $\ell = 29$. We show $D_\ell = \ell(\ell+1)C_\ell/(2\pi)$ as a function of the angular scale ℓ. [43]

The Cosmic Microwave Background is a faint glow of the era of decoupling of the early Universe (380000 years after the Big Bang). At this point in time the temperature of the Universe had dropped enough for electrons and protons to form hydrogen and the Universe became opaque to photons. This afterglow of recombination nowadays has an average temperature of 2.725 K, but small fluctuations are present. Figure 7 shows the angular power spectrum of these temperature fluctuations. It shows that the angular fluctuations with the largest amplitude lie around $\ell = 200$. At higher ℓ the amplitude peaks again at around $\ell = 700$ and $\ell = 850$, which implies that temperature fluctuation at this angular scale are louder than other angular scales. These peaks in the power spectrum give valuable information about the physics in the early Universe.

The first peak shows the imprint and oscillation pattern of sound waves in the baryon fluid in the early Universe. This fluid was affected by gravity and radiation pressure, which respectively pulled the fluid together or pushed it away. The pushing and pulling of radiation and gravity causes a profound oscillation pattern. The way this oscillation pattern is found in the CMB is affected by the curvature of the Universe. In a closed Universe the light from hot spots (large amounts of matter at the time of decoupling) will bend in such a way that they appear larger in the CMB, and vice versa. Comparing our expectations of the oscillation pattern at this scale and observations of the CMB we find that our Universe is flat [43].

The second and third peak contain information about the amount of regular and dark matter in the Universe. At these scales the oscillating pattern is being damped. This damping is due to diffusion of photons at the time of decoupling from matter. This decoupling process was not instantaneous but took a few tens of thousands of years. During this period, photons and other particles were still interacting, though not as frequently as before decoupling. This small interaction rate scattered the photons and therefore damped the imprint of the oscillation pattern at small scales. The amount of damping of the second and third peak compared to the first, gives insight in the amount of baryonic and dark matter in the Universe.

After decoupling from photons from matter, the Universe began its so-called Dark Age. This epoch is called Dark since there were only two radiation sources. One was the slowly redshifting CMB, the other were photons occasionally released by neutral hydrogen atoms. The latter mechanism is known as the 21 cm line of hydrogen. During the Dark Ages gravity was acting on matter to clump it in high density regions, that were able to form stars and galaxies. The Dark Ages slowly evolved into the next epoch, where actual stars and galaxies gradually formed. This lead to the event over reionization: the radiation of the first stars reionized the surrounding Universe. Neutral hydrogen atoms were split into a plasma of electrons and protons again. During this reionization the Universe remained largely transparent, and this epoch ended slowly due to the expansion of the Universe.

3.2   Dark matter annihilation at recombination - (Iris)

The structure and equations of this section are based on [39] and [44]. The annihilation of dark matter particles affects the ionization history of the Universe in three different ways. The interaction of the decay shower from the annihilation products with the thermal gas can either ionize the gas, induce a Ly-α excitation of hydrogen or simply heat the plasma. Figure 8 schematically shows the possible outcomes of dark matter annihilation. In this discussion we neglect the neutrino contribution, since they do not interact with the inter galactic medium (IGM). Ionization and Ly-α excitation influence the evolution of the free electron fraction x_e, while the heating of the plasma only affects the baryon temperature. Adjusting the expression for the evolution of the ionization fraction x_e for annihilation particles we find:

$$\frac{dx_e}{dz} = \frac{1}{(1+z)H(z)} \left[R_s(z) - I_s(z) - I_\chi(z) \right] \tag{11}$$

where R_s is the standard recombination rate, I_s the ionization rate by standard sources, and I_χ is the new term that accounts for the ionization rate due to particle annihilation. The first two terms are standard expressions, available in most CMB codes. See for example [45] and [46] which are based on [47].

The interesting addition to this equation is the ionization rate due to in this case the annihilation of dark matter particles. This ionization rate happens both by direct ionization from the ground state $(I_{\chi_i}(z))$ and by adding additional Ly-α photons to the plasma $(I_{\chi_\alpha}(z))$. These photons will increase the rate of photo-ionization by the CMB from the exited states. Therefore I_χ can be split up into two parts $I_\chi(z) = I_{\chi_i}(z) + I_{\chi_\alpha}(z)$.

The power output per unit volume by a self-annihilation dark matter particle is given by

$$\frac{dE(z)}{dV\,dt} = \rho_c^2 c^2 \Omega_{DM}^2 (1+z)^6 f \frac{<\sigma v>}{m_\chi} \qquad (12)$$

Figure 8: Figure from [48]: The injection of energy from dark matter annihilation into the IGM, via the creation of electromagnetic cascades. Energy transfer to the IGM takes place principally through the ionization and collisional processes.

As before $<\sigma v>$ is the effective velocity averaged cross section of the dark matter particle with mass m_χ. Ω_{DM} is the dark matter density parameter, ρ_c is the critical density of Universe today and the f parameter indicates the energy fraction that is absorbed overall by the gas. From here it is possible to relate $I_{\chi i}(z)$ and $I_{\chi \alpha}(z)$ to the power output:

$$I_{\chi_i} = C\chi_i \frac{[dE/dt]}{n_H(z)E_i}$$
$$\qquad\qquad\qquad\qquad\qquad\qquad (13)$$
$$I_{\chi_\alpha} = (1-C)\chi_\alpha \frac{[dE/dt]}{n_H(z)E_\alpha}$$

Here $\chi_i = \chi_\alpha = (1-x_e)/3$ are the fractions of energy going to ionizations and Ly-α photons respectively, $n_H(z)$ is the number density of hydrogen nuclei, E_i is the average ionization energy per baryon and E_α is the difference in binding energy between the 1s and 2p energy levels of a hydrogen atom. Incorporating formulae 12 and 13 in formula 11 yields a simple extension with the dark matter ionization rate to the standard evolution of the ionization fraction.

This extension of the ionization fraction is useful since we can compare it to current models and data and find how big certain dark matter parameters (such as $<\sigma v>$ and m_χ) can be before we find significant deviations from the CMB angular power spectrum. Therefore we can place upper limits on these parameters.

3.3 Sommerfeld enhancement - (Iris)

An example of the contribution of CMB analysis to our understanding of dark matter is the exclusion of Sommerfeld enhancement. In 2008 a positron excess was observed by the PAMELA satellite [49]. This excess was attributed to the signature of dark matter annihilation, where the dark matter cross section had to be enlarged via the Sommerfeld enhancement [50, 51]. In more recent work by [52] it is shown that dark matter annihilation can not be the cause of the positron excess. They conclude this based on the limits from the μ-type distortion of the CMB energy as observed by the FIRAS (Far Infrared Absolute Spectrophotometer) instrument on the COBE (Cosmic Background Explorer) satellite.
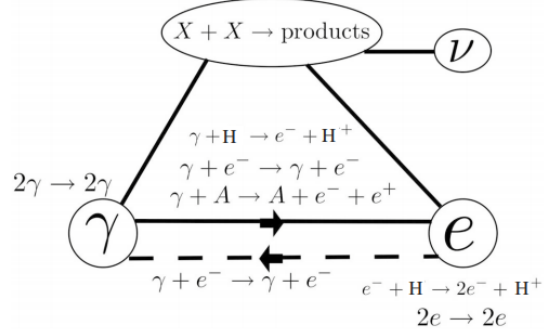
3.4 Cosmological signatures of dark matter self-annihilation - (Bouke)

Having discussed the theoretical link between dark matter annihilation and the thermal history of the Universe, we have all the tools we need to investigate potential footprints of the involved dark matter processes within acquired observational data. Of particular interest are the observations procured by the Planck satellite between 2009 and 2013. Having provided the highest sensitivity mappings of CMB anisotropies to date, this satellite has enabled researchers to put stringent upper limits on dark matter effective self-annihilation rates. Not surprisingly, in recent years we have seen the publication of several papers dedicated towards constraining dark matter annihilation parameters via Planck satellite data [53, 54]. This subsection is dedicated towards summarizing some of the most important findings.

3.4.1 Methodology

Before diving into the various results on dark matter self-annihiliation derived from cosmic microwave background data over the last years, let us first recapitulate on the methodology often applied in CMB indirect DM searches. In section 3.2 we saw that dark matter annihilation holds considerable sway over the course of cosmological history in the sense that the process may have injected vast amounts of energy into the intergalactic medium (IGM) at certain redshifts. From an observational point of view, this is important, since it might have lead to detectable defects in a diverse range of cosmological measurements, such as the baryonic matter and dark matter densities, the CMB angular power spectrum, the temperature of the intergalactic medium, as well as the optical depth towards the epoch of reionization. Of particular relevance to induced changes in all of these parameters, is the quantity:

$$p_{ann} \equiv f \frac{<\sigma v>}{m_\chi} \tag{14}$$

which was already encountered in equation 12. Since p_{ann} is directly coupled to the dark matter annihilation ionization rates by virtue of equation 11, the parameter will cause different evolution schemes of the free electron fraction x_e for different values. In the literature this is often modeled using the recombination coding routine *RECFAST* [55].
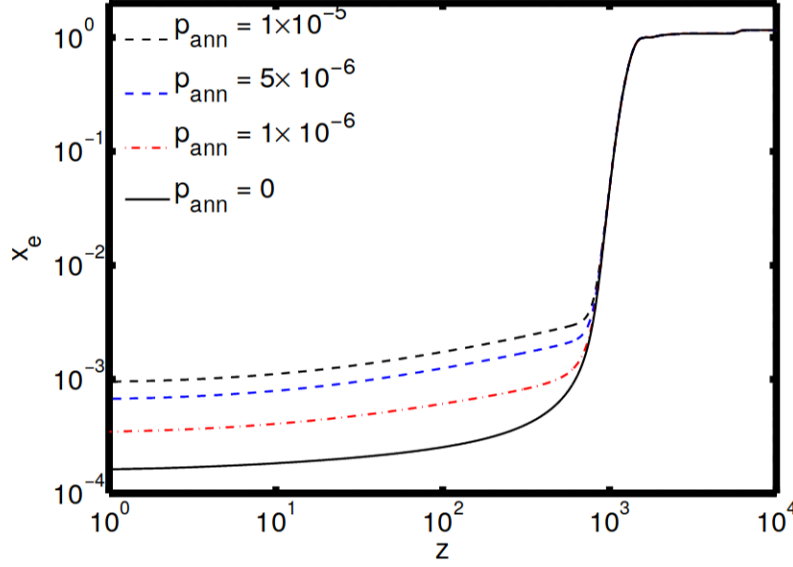
16

Figure 9: The evolution of the free electron fraction as a function of redshift for different values of $p_a nn$, as presented in Galli et al. (2009) [39].

Figure 9 displays the evolution of x_e for different values of p_{ann}. Evidently, values as small as $p_{ann} = 1 \times 10^{-5}$ can introduce up to an order of magnitude difference in the ionization fraction at redshifts $z < 10^3$ (before the epoch of recombination). This goes to show the impact that dark matter annihilation can have on cosmological history.

In close correspondence with the free electron fraction, the CMB angular power spectrum will also vary between different values of p_{ann}. This is perhaps best understood by looking at optical depth. If the number density of free electrons is indeed enhanced by dark matter self-annihilation, the optical depth towards the last scattering surface of the CMB photons will naturally increase. As a consequence we will have to deal with a larger opacity when measuring the CMB, causing the amplitude in the angular power spectrum to decrease.

Figure 10 displays how the temperature (TT) and E-mode polarization (EE) CMB angular power spectra as well as the temperature and E-mode polarization cross spectrum (TE) vary for different dark matter annihilation schemes. As we predicted earlier, the acoustic oscillations within the angular power spectra become damped whenever there is a non-trivial dark matter annihilation rate. More interesting to note is the fact that there exists little difference between the curves with equivalent values of $< \sigma v > / m_\chi$. This has to do with the fact that the f-parameter in equation 14 varies very little over the redshift range where scattering of CMB-photons is most likely (i.e. between around $z \sim 800$ and $z \sim 1200$[3]). As a consequence, the acoustic oscillations of the power spectra are only truly affected by the average value of f around $z \sim 1100$, which happens to be nearly equal for all dark matter WIMP candidates with equal annihilation-rate-to-mass ratio $< \sigma v > / m_\chi$.

> Perhaps this should be properly explained

In order to formulate a definitive answer to the question which model for dark matter annihilation holds the most merit (i.e. which value of p_{ann} yields the most sensible numbers for CMB observables), one has to confer with observational data in some way or another. Usually this is accomplished via a

---

[3]This is explained in more detail Hütsi et al. (2011) [56]. In particular, see the sharp peak of the visibility function around $z \sim 1100$ in figure 2 of the same paper.
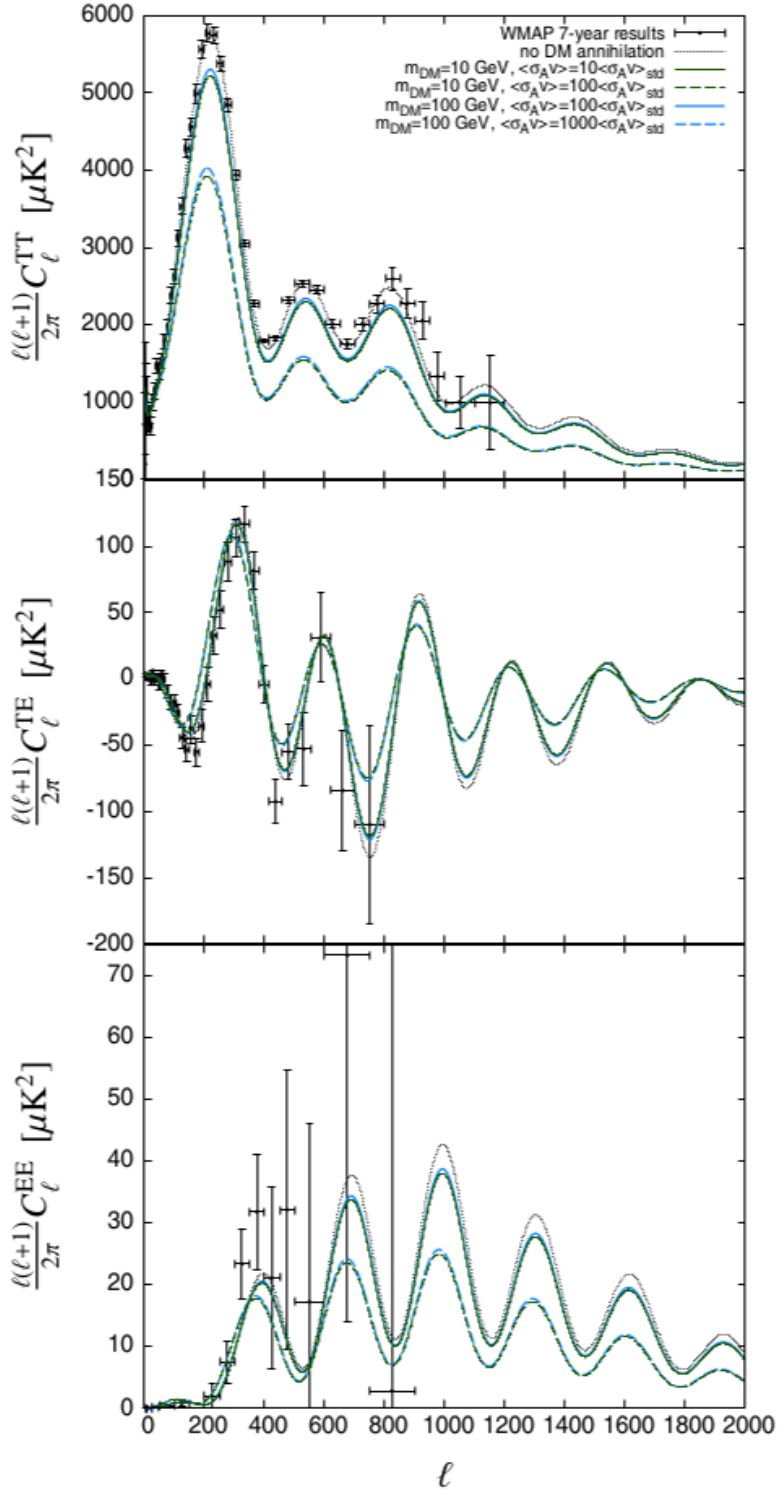
Figure 10: Angular power spectra of the CMB as presented in Hütsi et al. (2011) [56] for different dark matter masses and annihilation rates. From top to bottom we have (i) the angular power spectra derived for the CMB temperature anisotropies, (ii) the temperature and E-mode polarization cross-spectra and (iii) the E-mode polarization spectra. Dotted lines show theoretical predictions for the ΛCDM model [57], whilst the points with errorbars indicate 7-year measurements conducted by the WMAP space mission.

series of maximum likelihood fits to the parameters:

$$\{\Omega_{b,0}h^2, \Omega_{DM,0}h^2, \Theta_s, z_{reio}, n_s, \ln\left[10^{10}A_s\right], <\sigma v>, m_\chi\} \tag{15}$$

where $\omega_b \equiv \Omega_{b,0}h^2$ stands for the baryonic matter density, $\omega_{DM} \equiv \Omega_{DM,0}h^2$ denotes the dark matter density and Θ_s describes the ratio between the angular sound horizon and the angular diameter to decoupling[4]. Furthermore, z_{reio} stands for the redshift to the start of reionization, n_s indicates the scalar spectral index, $\ln\left[10^{10}A_s\right]$ indicates the logarithmic amplitude of the primordial power spectrum[5], $<\sigma v>$ denotes the thermally-averaged dark matter annihilation cross section and m_χ describes the dark matter mass. A Markov Chain Monte Carlo (MCMC) analyzation method allows one to sample values for each of the cosmological parameters ω_b, ω_{DM}, Θ_s z_{reio}, n_s and A_s, such that WMAP and PLANCK CMB observational data are fitted best.

In figure 11 we see the constraints derived by Galli et al. for the baryonic and cold dark matter density as well as the scalar spectral index using the five-year WMAP satellite data in 2009. Although the cold dark matter density does not seem to be affected by the inclusion of dark matter annihilation, the baryonic matter density and the scalar spectral index are clearly subjected to a shift. For an upper limit $p_{ann} < 2.0 \times 10^{-6}\,\mathrm{m}^3/\mathrm{s/kg}$ we see that the constraint on ω_b changes from $\omega_b = 0.0228 \pm 0.0006$ to $\omega_b = 0.0230 \pm 0.0006$, whilst the limits on n_s change from $n_s = 0.965 \pm 0.014$ to $n_s = 0.977 \pm 0.018$.

These results conform to what one might expect qualitatively. After all, in the presence of dark matter annihilation into standard model particles, the overall baryonic matter content of the Universe ought to increase. Furthermore, the net decrease in dark matter during the period of inflation, will result in generally greater density fluctuations, since the gravitational potential associated with regional matter overdensities will decrease. This yields a larger value of n_s, which is reflected by the graph in figure 11.

Some more recent papers, incorporating the latest data by WMAP and PLANCK give constraints on $\ln\left[10^{10}A_s\right]$ and the IGM temperature T_m, similar to the ones discussed above for n_s, ω_b and ω_c. Of particular interest are figures 12 and 13, which can be found in Lopez-Honorez (2013) [59] and in Madhavacheril et al. (2014) [54] respectively. As can be seen, lower dark matter particle masses and higher annihilation rates lead to higher IGM temperatures. This makes sense, considering that greater values of p_{ann} lead to increased energy injection rates, as we saw previously in equation 12. Another interesting fact to note is that the dark matter annihilation rate decreases, whenever the dark matter particle mass goes down (see the brown datapoints in the plot). This is of course caused the decrease in energy phase space, which makes the annihilation process less efficient.

_A_s, n_s and Θ_s should perhaps be explained in more detail in the introduction to this chapter._

incorporate comments from presentation

Discuss 13 in more detail

---

[4]With *the sound horizon* we refer to the characteristic length scale of the CMB accoustic oscillations, which are given by the comoving distance that a sound wave can travel between the Big Bang and recombination [58].

[5]The *scalar spectral index* n_s and the amplitude A_s usually come up when discussing primordial density fluctuations. In this context, the power in density fluctuations with wavenumber k is generally assumed to behave as $P(k) = A_s(k/k_\star)^{n_s-1}$, where $k_\star = 0.05\,\mathrm{Mpc}^{-1}$ denotes a reference scale and where $n_s = 1$ corresponds to a situation of *scale-invariant* fluctuations.
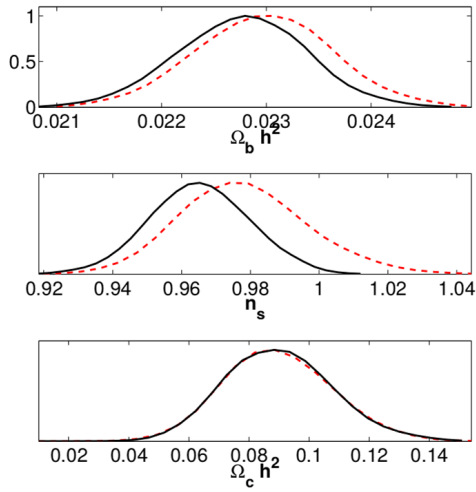
Figure 11: The 1-D likelihood distributions of the baryonic matter density, the scalar spectral index and the cold dark matter density as derived in Galli et al. (2009) [39] using the five-year WMAP dataset. Solid lines indicate results in the case of standard recombination, whilst dasheed lines show constraints including dark matter annihilation.
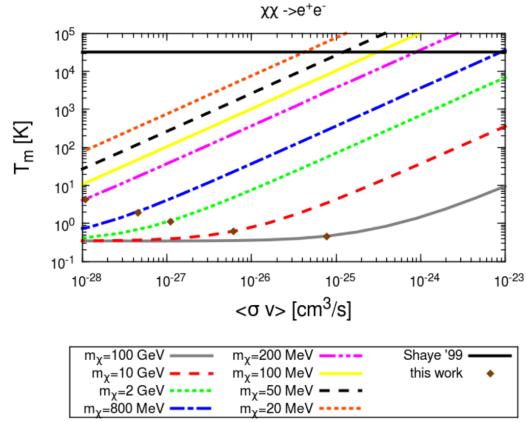
Figure 12: Dark matter annihilation constraints on the IGM temperature T_m as presented in Lopez-Honorez (2013) [59], assuming annihilation occurs into e^+e^- pairs solely and $z_{reio} = 10$. Brown diamond indicate upper limits obtained for $< \sigma v >$ using WMAP9+SPT11+HST+BAO data, whilst a black solid line shows the $T_m = 32\,000\,\mathrm{K}$ upper limit derived from Ly-α observations at $2 < z < 4.5$.
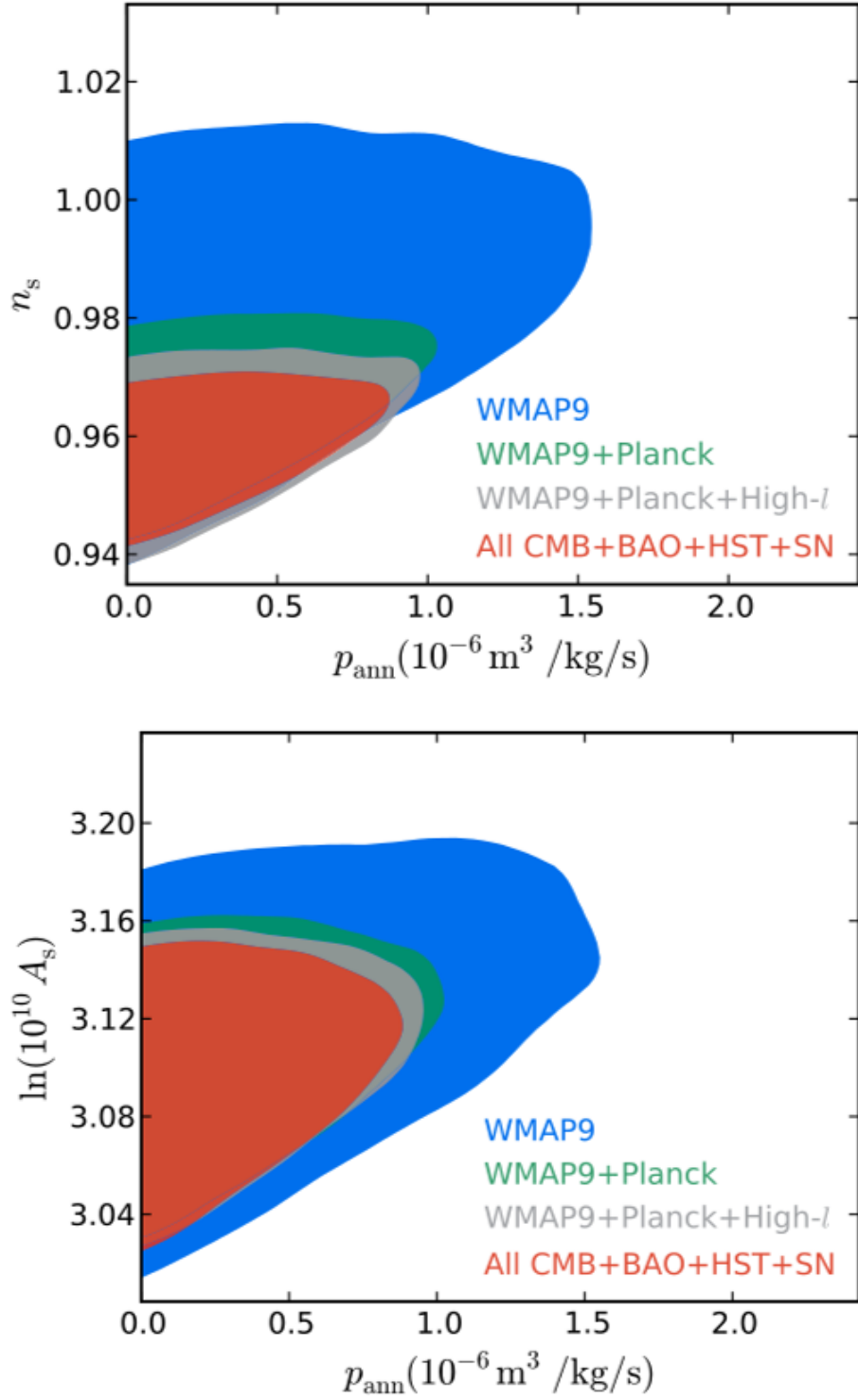
Figure 13: 95% confidence limit contours for n_s and $\ln\left[10^{10} A_s\right]$ as a function of p_{ann} as derived by Madhavacheril et al. in 2014 [54] for selected combinations of datasets.

3.5 Observational constraints of self-annihilation cross section from WMAP and PLANCK data - (Paul)

From the constraints on p_{ann} that come from maximum likelihood parameter fitting (see chapter 3.4.1) and using equation 14, we find the following velocity averaged annihilation cross section $< \sigma v >_r$ at recombination as a function of dark matter mass m_χ, see figure 14. Note that f the coupling between the galactic gas with the dark matter annihilation product depends on multiple less understood factors; composition of the shower, its energy spectrum and most likely on the properties of the dark matter particles itself. In figure 14, the coupling factor is set to $f = 0.5$, which seems to be a good average approximation over different channels by [39]. It is clear that finding these constraints for different values of f should not be a problem, and is therefore less relevant.
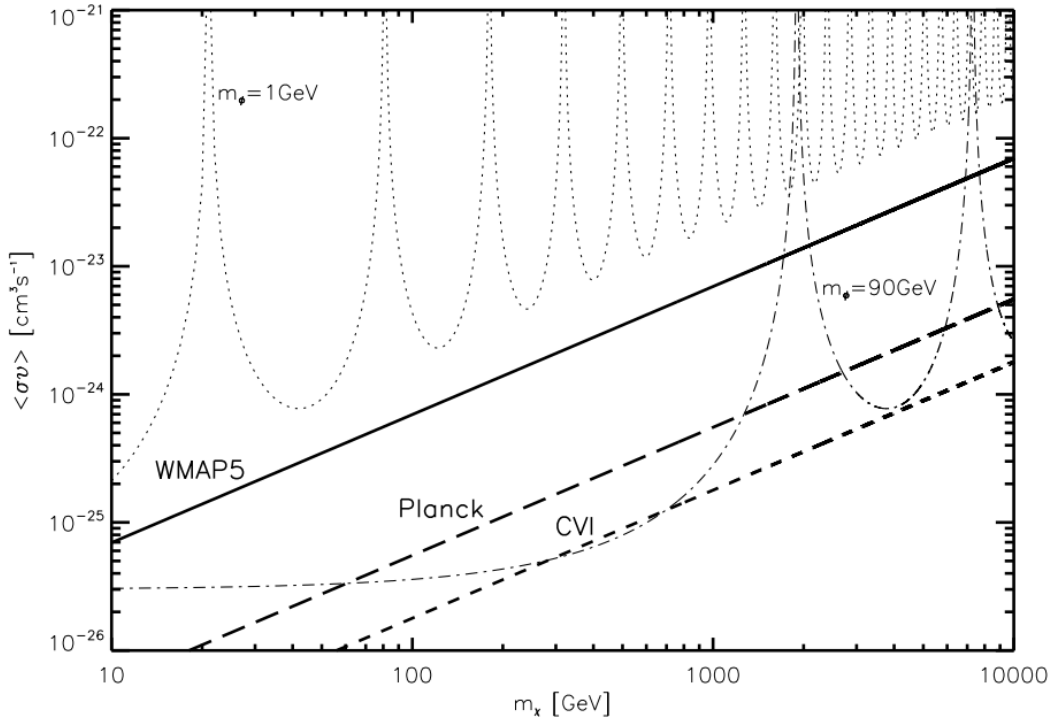
Figure 14: Figure from [39]. Velocity averaged annihilation cross section $< \sigma v >_r$ at recombination as a function of dark matter mass m_χ, with the coupling parameter $f = 0.5$. Where the thin dashed lines are constraints from Sommerfeld enhanced cross sections (for two different boson masses $m_\phi = 1$ GeV and $m_\phi = 90$ GeV) and the thick lines are constrains from WMAP and predicted Planck data and its Cosmic Variance Limited case.

The thin dashed lines correspond to the constrains by the Sommerfeld enhancement (SE), which enhances the self-annihilating dark matter cross section to explain the positron excess mentioned before (see chapter 3.3). This has been plotted for two different force carrier boson masses ($m_\phi = 1GeV$ and $m_\phi = 90GeV$). The resonating form of the constraints is due to the Sommerfeld enhancement solution being saturated at low velocity ($\beta \sim m_\phi/m_\chi$), see formula 16.

$$SE(\beta) = \frac{\alpha\pi}{\beta}\left(1 - e^{-\alpha\pi/\beta}\right) \tag{16}$$

The thick line describes the constrains found from the WMAP5 data (2009) [60] and their maximum likelihood fits of the parameters found in 15. It also excludes most of the Sommerfeld enhancements

22

in the boson mass range of a few GeV. We can summarize the WMAP5 constraints by the following upper limit cross section:

$$\sigma v_{z_r}^{max} = 71.2 \cdot 10^{-26} \Big(\frac{p_{ann}^{max}}{2.0 \cdot 10^{-6} m^3 s^{-1} kg^{-1}} \Big) \Big(\frac{m_\chi}{100 GeV} \Big) \Big(\frac{0.5}{f} \Big) \tag{17}$$

Where $\sigma v_{z_r}^{max}$ is the upper limit on the velocity averaged self-annihilation cross section in terms of p_{ann} equation 14, m_χ the dark matter WIMP mass and f the coupling factor.

A prediction of the probe qualities of Planck (2015) is plotted as the thick long dashed line. Planck data is discussed more in-depth below. The Cosmic Variance Limited (CVL) case with comparable angular resolution as Planck, is also plotted and denoted as the thick short dashed line. In the CVL case, the Gaussian like fluctuations of the cosmic microwave background are ignored, which almost differ a order of magnitude with the real constraints. Figure 14 also shows that for increasing dark matter mass m_χ, the cross section also goes up as you would expect from equation 17. In the previous method of detecting dark matter (see chapter 2) we saw that probing higher masses is difficult due to a low gamma-ray flux.

3.5.1 WMAP

The Wilkinson Microwave Anisotropy Probe (WMAP) launched on a spacecraft in 2001 by NASA into a lunar assisted trajectory (see Appendix 6.1) and was the successor of COBE. It was planned to observe the CMB fluctuations for 24 months, which was subsequently extended to almost 10 years. The passively cooled microwave radiometers measure the temperature difference of the CMB between two different points in the sky and compares them directly. This method is more accurate than measuring absolute values and allows WMAP to probe up to $0.0002K$ differences over a frequency range of $23-94GHz$ (see NASA website [61]). It's 5 year run data (WMAP5) provides stringent constraints on the parameters of the minimal ΛCDM model [60], which are shown in figure 15. The uncertainties on these parameters are partly due to instrumental effects but largely due gravitational lensing by imhomogeneous mass distributions in or along the line of sight.

SUMMARY OF THE COSMOLOGICAL PARAMETERS OF ΛCDM MODEL AND THE CORRESPONDING 68% INTERVALS

Class	Parameter	WMAP 5-year ML[a]	WMAP+BAO+SN ML	WMAP 5-year Mean[b]	WMAP+BAO+SN Mean
Primary	$100\Omega_b h^2$	2.268	2.262	2.273 ± 0.062	$2.267^{+0.058}_{-0.059}$
	$\Omega_c h^2$	0.1081	0.1138	0.1099 ± 0.0062	0.1131 ± 0.0034
	Ω_Λ	0.751	0.723	0.742 ± 0.030	0.726 ± 0.015
	n_s	0.961	0.962	$0.963^{+0.014}_{-0.015}$	0.960 ± 0.013
	τ	0.089	0.088	0.087 ± 0.017	0.084 ± 0.016
	$\Delta_\mathcal{R}^2(k_0{}^e)$	2.41×10^{-9}	2.46×10^{-9}	$(2.41 \pm 0.11) \times 10^{-9}$	$(2.445 \pm 0.096) \times 10^{-9}$
Derived	σ_8	0.787	0.817	0.796 ± 0.036	0.812 ± 0.026
	H_0	72.4 km/s/Mpc	70.2 km/s/Mpc	$71.9^{+2.6}_{-2.7}$ km/s/Mpc	70.5 ± 1.3 km/s/Mpc
	Ω_b	0.0432	0.0459	0.0441 ± 0.0030	0.0456 ± 0.0015
	Ω_c	0.206	0.231	0.214 ± 0.027	0.228 ± 0.013
	$\Omega_m h^2$	0.1308	0.1364	0.1326 ± 0.0063	$0.1358^{+0.0037}_{-0.0036}$
	$z_{\text{reion}}{}^f$	11.2	11.3	11.0 ± 1.4	10.9 ± 1.4
	$t_0{}^g$	13.69 Gyr	13.72 Gyr	13.69 ± 0.13 Gyr	13.72 ± 0.12 Gyr

[a]Dunkley et al. (2008). "ML" refers to the Maximum Likelihood parameters
[b]Dunkley et al. (2008). "Mean" refers to the mean of the posterior distribution of each parameter
[c]Dunkley et al. (2008). "ML" refers to the Maximum Likelihood parameters
[d]Dunkley et al. (2008). "Mean" refers to the mean of the posterior distribution of each parameter
[e]$k_0 = 0.002$ Mpc^{-1}. $\Delta_\mathcal{R}^2(k) = k^3 P_\mathcal{R}(k)/(2\pi^2)$ (Eq. [15])
[f]"Redshift of reionization," if the universe was reionized instantaneously from the neutral state to the fully ionized state at z_{reion}
[g]The present-day age of the universe

Figure 15: Table from [60]. Maximum likelihood parameters of ΛCDM model by WMAP5, BAO and SN data set.

Some of the parameters mentioned in 15 can be directly found in figure 15; Hubble constant H_0 and h, baryonic matter density Ω_b, dark matter density Ω_c, scalar spectral index n_s and the z value of reinozation z_{reion}. Also found in [60] is the amplitude of the primordial power spectrum $A_{ps} = 0.0011 \pm 0.001 \mu K^2 sr$, they leave the parameters $<\sigma v>_r$ and m_{DM} to others.

3.5.2 Planck

The successor of WMAP is named after the German Nobel prize winner; Max Planck. It is also the first probe send by the European Space Agency (ESA) which focuses on studying the CMB. Planck launched in 2009 and orbits the second liberation point (L2) just like WMAP did, see Appendix 6.1. Furthermore, Planck observers in a frequency range of $30 - 857 GHz$ in nine frequency ranges instead of five for WMAP, which improve the astrophysical foreground models. Understanding the imhomogeneous mass distributions in and along the line of sight is quite important, since the measurement will be limited by how well the foreground can be subtracted. After a three year run, to following constraints on the ΛCDM model parameters were found [43]:

Parameter	PlanckTT+lowP 68% limits	PlanckTT, TE, EE+lowP 68% limits
$\Omega_b h^2$	0.02222 ± 0.00023	0.02225 ± 0.00016
$\Omega_c h^2$	0.1197 ± 0.0022	0.1198 ± 0.0015
$100\theta_{MC}$	1.04085 ± 0.00047	1.04077 ± 0.00032
τ	0.078 ± 0.019	0.079 ± 0.017
$\ln(10^{10}A_s)$	3.089 ± 0.036	3.094 ± 0.034
n_s	0.9655 ± 0.0062	0.9645 ± 0.0049
H_0	67.31 ± 0.96	67.27 ± 0.66
Ω_Λ	0.685 ± 0.013	0.6844 ± 0.0091
Ω_m	0.315 ± 0.013	0.3156 ± 0.0091

Figure 16: Table from [43]. Constraints on the cosmological ΛCDM model by Planck.

The results of WMAP and Planck agree with each other, but more impressive are the two to three order of magnitude improvements on the uncertainties of the parameters. Table 17 shows consistent output parameters under different maximal likelihood methods. These results also show a remarkable agreement considering different foreground approximations have been used. [43].

Parameter	Plik	CamSpec	Hillipop	Mspec	Xfaster (SMICA)
$\Omega_b h^2$	0.02221 ± 0.00023	0.02224 ± 0.00023	0.02218 ± 0.00023	0.02218 ± 0.00024	0.02184 ± 0.00024
$\Omega_c h^2$	0.1203 ± 0.0023	0.1201 ± 0.0023	0.1201 ± 0.0022	0.1204 ± 0.0024	0.1202 ± 0.0023
$100\theta_{MC}$	1.0406 ± 0.00047	1.0407 ± 0.00048	1.0407 ± 0.00046	1.0409 ± 0.00050	1.041 ± 0.0005
τ	0.085 ± 0.018	0.087 ± 0.018	0.075 ± 0.019	0.075 ± 0.018	0.069 ± 0.019
$10^9 A_s e^{-2\tau}$	1.888 ± 0.014	1.877 ± 0.014	1.870 ± 0.011	1.878 ± 0.012	1.866 ± 0.015
n_s	0.962 ± 0.0063	0.965 ± 0.0066	0.961 ± 0.0072	0.959 ± 0.0072	0.960 ± 0.0071
Ω_m	0.3190 ± 0.014	0.3178 ± 0.014	0.3164 ± 0.014	0.3174 ± 0.015	0.3206 ± 0.015
H_0	67.0 ± 1.0	67.1 ± 1.0	67.1 ± 1.0	67.1 ± 1.1	66.8 ± 1.0

Notes. Each column gives the results for various high-ℓ TT likelihoods at $\ell > 50$ when combined with a prior of $\tau = 0.07 \pm 0.02$. The SMICA parameters were obtained for $\ell_{max} = 2000$.

Figure 17: Table from [43]. Constraints on the cosmological ΛCDM model with Planck data, analyzed by different maximal likelihood methods.

4 Dark matter detection with anti-matter

In the previous sections of this review on indirect searches for dark matter, we focused our attention on signatures observable in the electromagnetic spectrum. So far we've looked at potential signals in the gamma-ray spectrum and in the CMB. However, with the construction of large new facilities for observing cosmic rays and neutrino's and with the recent confirmation of the existence of gravitational waves, it is important that we also look at non-EM observables. The following section will be dedicated to cosmic-ray dark matter signatures. In particular we'll explore how excess levels of positrons and antiprotons might be interpreted as secondary products of dark matter annihilation.

4.1 The Positron channel - (Bouke)

When the PAMELA collaboration published their results on the cosmic positron flux back in 2008, excitement was felt accross the entire astrophysical community: an excess signal above 7 GeV seemed to be compatible with expectations for dark matter annihilation, which would make Pamela the first instrument to indirectly confirm the existence of dark matter WIMPS. How were scientists at the time so convinced of having found a dark matter signature? And why were the claims originally made, subsequently toned down? In the following section, an attempt is made to give an answer to both of these questions via analysis of recent literature. First, we'll discuss the general background of the problem, as well as the values one might expect to observe for the positron and electron+positron flux, both in case of the absence of dark matter and in its presence. Afterwards several different experimental results will be presented, which show how observations deviate from a pure background scenario. The final paragraphs will consist of an overview of several debates which ensued in the literature, contesting original the original claims made of dark matter indirect detection.

4.1.1 Expectations for the positron fraction and the electron+positron flux

The claim that there exists an 'excess' flux of positrons in observed cosmic ray spectra, of course begs the question in which respect observed signals are in transgression. The answer is not immediately obvious and, consequentially, several authors have tried to explain the rising fraction of positrons as a spectral feature instead of a true anomaly [62]. To illustrate these different viewpoints, let us look at a more quantitative description of the problem. The positron fraction of cosmic rays can be modelled using the formula [63]:

$$f(E) \equiv \frac{1}{1 + (\Phi_{e^-}/\Phi_{e^+})} \approx \frac{1}{1 + \kappa E_{\text{GeV}}^{\rho}} \tag{18}$$

where the fluxes Φ_{e^-} and Φ_{e^+} for electrons and, respectively, positrons signify values measured at the top of the atmosphere and where E_{GeV}^{ρ} denotes the fractional (power-law) energy spectrum of electrons versus positrons for spectral index ρ, with κ serving as the necessary constant of proportionality to fix dimensionality. Simple fits to PAMELA data above 10 GeV[6] yield $\rho = -0.38 \pm 0.06$ in case of the original analysis provided in 2009 [64], or $\rho = -0.23 \pm 0.04$ for the more recent analysis presented by the PAMELA collaboration in 2010 [65]. At the same time, fits to PAMELA electron data over the same energy interval show that $\Phi_{e^-} \propto E^{-3.23 \pm 0.02}$, which would imply that $\Phi_{e^+} \propto E^{-2.85 \pm 0.06}$ (or $\Phi_{e^+} \propto E^{-3.00 \pm 0.04}$ in case of the 2010 analysis). However, if this is the case, the proton flux measured by PAMELA would be in disagreement. To understand this, it is important to keep in mind that all ISM positrons trace their origins back to positrons. Hence, discrepancies between the spectral indices of these two particles hint at the occurrence of some underlying process.

Recent PAMELA measurements of the positron flux indicate that the proton cosmic ray spectrum behaves as $\Phi_p \propto E^{-2.82}$. At first glance, this seems to be in reasonable agreement with the earlier stated spectral behaviour of Φ_{e^+}. However, propagation phenomena haven't been taken into account yet.

---

[6]Incorporating data below this threshold would include charge-dependent solar modulation effects, which are detrimental to the accurate determination of the cosmic positron flux.

These generally tend to cause spectral steepening and therefore cannot be kept out of the picture. Assuming, propagation happens via diffusive channels alone, one would expect to see the positron spectral index drop by about $\delta \approx 0.4$ [66]. But effects may be even more dramatic in the TeV-regime, where diffusion can drive fluxes of leptons down by as much as $\tilde{1}$, assuming a leaky box model dominated by radiative loss . In a recent numerical analysis conducted by J. Lavalle in 2011 [67] the positron cosmic ray flux is therefore situated at $\Phi_{e+} \propto E^{-3.4}$ in the 10-100 GeV range, which clearly violates the spectral behaviour inferred from PAMELA observations. As a consequence, we often speak of an excess or 'anomaly' of positrons measured with respect to the expected positron fraction from numerical simulations. It is worthy to keep in mind, however, that the discrepancy between observational data and prospected values for Φ_{e+}, may also be caused by some mistake in our current theoretical models for cosmic ray propagation. This would perhaps even offer for a breakthrough of greater extent than the addition of new primary cosmic ray sources. Nevertheless, despite several concerns raised with our current theoretical understanding of the problem [**?**] , the notion of additional primary sources stands tall, since no propagation mechanisms are known which could steepen the positron spectrum between 10 GeV and 100 GeV by less than 0.2 with respect to its primary (i.e. proton) counterpart.

Is this also in [25] (Berezinsky et al. 1990)?

include proper citation in ref.bib

Assuming that the steepening of the positron spectrum above 10 GeV is not caused by any unknown propagation effects, the next question to tackle would of course be what phenomenon actually might be responsible for the measured excess. Over the years a variety of different explanations have come up. In 2009, Shaviv et al. proposed a model in which the surplus positron fraction may be attributed to a non-conventional shape of the electron flux, caused by e.g. the sum of a diffuse disk population and a local one [69]. However, even though it is likely that lepton propagation becomes anisotropic at high energies (even below the TeV scale) this model is strongly disfavoured by present data (see for example the analysis given by J. Stockton in 2011 [70]). Hence, using Ockham's razor, the best (i.e. simplest and most conservative) explanation for the measured excess of positrons seems to be that there exists a population of primary positron accelerators.
Support for the primary positron accelerator scenario comes in the form of recent Fermi measurements. Besides detecting a positron spectrum harder than $E^{-3.0}$ in the range of interest [71], one component fits of Fermi data fail to reproduce both the total $e^+ + e^-$ fluxand the e^+ flux. This suggest that proton contamination cannot be the main source of the observed anomaly. More importantly, however, it also provides support for the existence of an additional electron-positron production channel. In the following paragraphs we'll investigate the various astrophysical sources cited as potential sites for such production.

4.1.2 Dark Matter annihilation

The 2008 PAMELA collaboration release on the measured overabundance of positrons sparked a lot of interest in the particle physics community since 'excess' abundances of positrons are qualitatively expected in most dark matter annihilation models. As for the reason why the paper hasn't been unanimously brought forward as the first ever description of indirect dark matter detection, we can point at three observational caveats.
One of the main causes behind the ongoing debate surrounding the dark matter interpretation of the positron excess is given by the absence of a sharp spectral edge after the initial rise which is observed. In case the measured anomaly is indeed caused by dark matter annihilation, such an edge would be expected. However, it has not been observed as of present, neither in the e^+ fraction nor as a dip in the $e^+ + e^-$ data. A second cause for worry is provided by the surprisingly large normalization factor the dark matter contribution would be associated with, compared to predictions for typical S-wave annihilation thermal relics in agreement with observed dark matter abundances ($\langle \sigma v \rangle \gg \langle \sigma v \rangle_{th,S-wave} \approx 1\,\mathrm{pb}$) Thirdly, the large flux of electron-positron pairs observed by PAMELA implies the existence of similar excesses in the spectra of other high-energy particles, such as antipro-
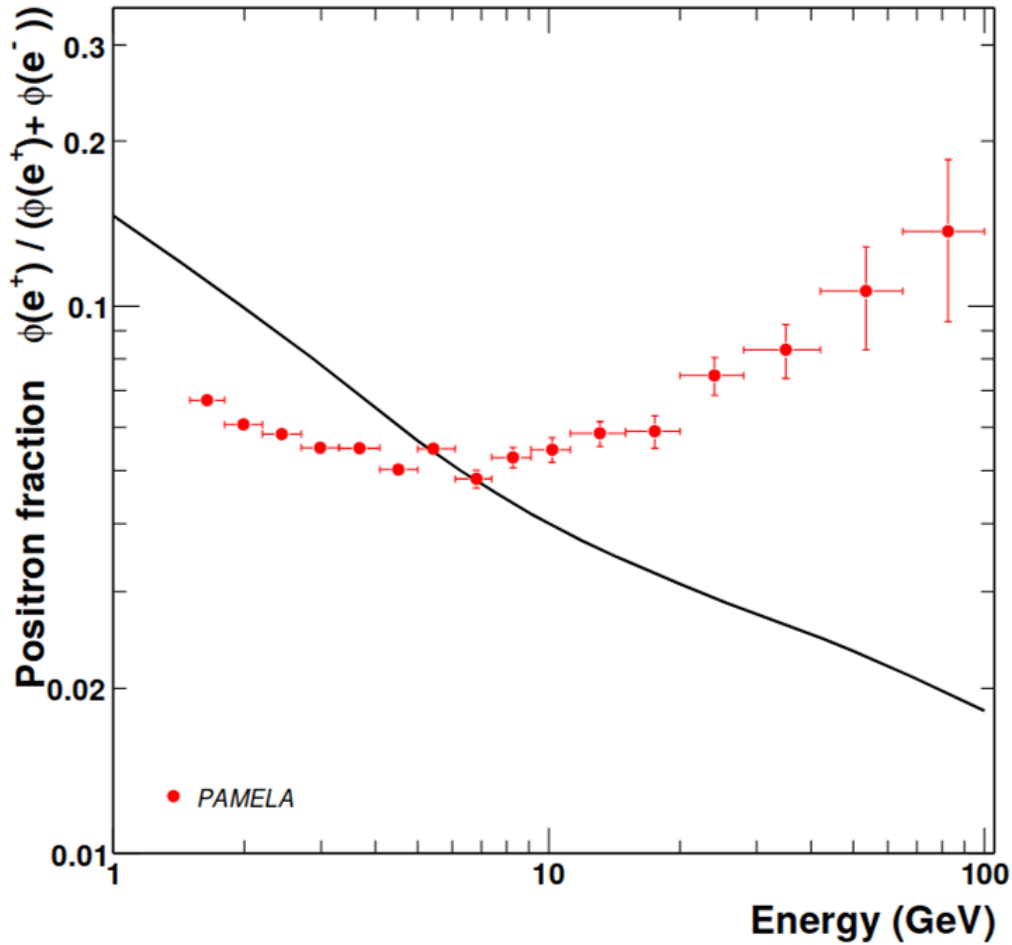
Figure 18: The PAMELA positron fraction as presented in the original 2008 PAMELA paper on the anomalous positron abundance [64]. A solid line indicates a theoretical prediction done by Moskalenko and Strong for pure secondary production of positrons during the propagation of cosmic rays through intergalactic space [68].

tons, gamma-rays and possibly neutrinos, whilst no such anomalies have been yet been revealed.

There are several ways to overcome the above difficulties, such that the dark matter annihilation picture can be maintained. The first is to increase the dark matter mass m_χ to values above the range accessible to PAMELA. Although this solves the first of the three mentioned problems, it may further complicate the second and third issues. After all, since the differential spectrum from dark matter annihilation scales as m_χ^{-2} (confer with equation **??** for a similar dependency in the case of the dark matter-induced gamma-ray flux), we would need an even higher annihilation rate $\langle \sigma v \rangle$ than before to achieve the same observational positron fluxes. Putting this aside for the moment, however, there are three ways in which the problem surrounding the exceptionally high annihilation rate may be remedied:

1. The first method is to attribute the high positron flux to a nearby clump of dark matter (as suggested in, for example, Hooper et al. (2009) [72]). In our current understanding of structure

27

formation, however, this scenario seems very unlikely, especially given the constraints derived from gamma-ray fluxes in recent years.

2. The second option would be simply to accept that $\langle \sigma v \rangle \gg 1$ pb and try to explain the high value from an underlying physical process. One of the most popular methods cited in line with this approach, is the so-called Sommerfeld enhancement, which we also mentioned in the context of the previous chapter. Basically this enhancement constitutes an increase of the dark matter annihilation cross section as an effect of long-range (i.e. below TeV^{-1} scale) attractive forces, which are expected to operate within low-velocity (i.e. $v \approx 1 \times 10^{-3}$ c regimes). Several alternatives to the Sommerfeld enhancement scheme include: a) non-thermal dark matter candidates, whose production is dictated by decays of other species and condensates rather than thermal freeze-out, b) a Breit-Wigner resonant enhancement and c) a different theoretical framework for cosmological evolution of particle populations altogether. Take in mind that all of these options require some form of ad hoc parameter tuning, `[what is this?]`

3. The third solution is provided by positron production channels which originate from dark matter decay, instead of dark matter annihilation. Although this scenario may explain measured excesses quite neatly, it isn't favoured from an observational point of view, since the corresponding lifetime of $\approx 1 \times 10^{26}$ s required to fit the data cannot be predicted beforehand. Rather it has to be inferred a posteriori. Similar to the sec

Although a detailed analysis of the various considerations presented here, lies beyond the scope of this review, we should note that each model comes with a variety of different cavities of its own. The best way forward in pinning down the intricacies of dark matter annihilation seems to be to combine the different pictures and observational data that are currently available. Hence, good models for the positron excess should incorporate the stringent limits provided by the CMB, as well as current constraints derived from cosmic-ray fluxes.

4.1.3 Other potential sources: pulsars and pulsar wind nebulae

Although dark matter annihilation provides one of the most exciting explanations for the positron excesses measured by cosmic-ray observatories, it is possible to conceive of a variety of other phenomena resulting in the same behaviour. One of the most prominent alternative sources for positron cosmic-rays, often cited in the literature, are pulsars. Essentially consisting of rapidly spinning, magnetized neutron stars with highly relativistic jets, these objects might constitute some of the primary loci of cosmic-ray leptons in the Universe: since the objects have extremely high rotation rates, electrons are theorized to be kinematically stripped from the stellar surface under the influence of large induced tangential electric fields [73]. This effect is, in fact, so strong that neutron stars are generally believed to be surrounded by spherical clouds of comoving plasma called "magnetospheres" up to typical distances known as the light radius $r_L = c/\Omega$. The electrons that end up within this sphere subsequently undergo radiative cooling (particularly via synchrotron radiation), producing very high energy photons in the process. In turn, these created photons may contribute to pair-production, resulting in the formation of electron-positron pairs. `[Under construction]`

4.2 Antiproton channel - (Iris)

An other way to search for dark matter annihilation is via the the antiproton spectrum. Antiprotons can result either from the hadronization of primary quarks or gauge bosons or via electroweak radiation from leptonic channels. This idea is 30 years old already [74], but due to improvements in observations we are able to put stronger constraints on the dark matter parameters. In this section we will discus the CR antiproton flux. The dark matter interpretations of the leptonic excesses (see section 4.1) are usually not favoured over explanations involving astrophysical sources [75]. In the interpretation of the CR antiproton flux, the secondary antiprotons have been shown to account for most of the measured flux [76]. This allows us to derive strong constraints on the dark matter contribution to the antiproton flux.

The Alpa Magnetic Spectrometer (AMS-02) onboard the ISS, is the most advance detector of charged cosmic ray (CR) flux and therefore one of the most detectors in indirect dark matter experiments. Its most recent results provide the best measurements of the antiproton-to-proton flux ration to date [77]. The new AMS-02 data furthermore improves the measurements of the proton spectrum and helium one. These measurements agree with previous publications by an other CR flux detector, PAMELA [78], but are more precise and detailed. These two quantities are important ingredients in the computation of the secondary antiproton flux, which is the minimal astrophysical antiproton background in indirect dark mater research.

4.2.1 Astrophysical antiproton background

Secondary antiprotons are produced when CR high energy protons and helium nuclei collide with the interstellar medium. The interstellar medium consist mainly of hydrogen and helium, heavier nuclei corrections are only a few percent (see section 4.3). To compute the secondary astrophysical antiproton flux we require: i) the injection of proton and helium fluxes from Galactic sources ii) the collision cross section and iii) the propagation details. For the proton and helium spectra the newest AMS-02 data are used. These measurements have some uncertainties that translate into the $\bar{p}/p$ ratio, as shown in the blue uncertainty band of figure 19. The spectra are measured up to a rigidity $(R = B \cdot r_{gyro})$ of 1.8 and 3 TV for protons and helium respectively. Both of these spectra are best described by a broken power-law, with the break around $R \sim 300$ GV. The most important collision cross sections for the antiproton production are the following including their contribution to the total antiproton production: $\sigma_{p,H \to \bar{p}}$ (60-65%), $\sigma_{p,He \to \bar{p}}$, $\sigma_{He,H \to \bar{p}}$ (together 32-37%) and $\sigma_{He,He \to \bar{p}}$ ($< 3\%$). Taking into account all the uncertainties on these cross sections, we find the uncertainty band for the astrophysical $\bar{p}/p$ ratio. as shown in the red uncertainty band of figure 19. By semi-analytically solving the full transport equation for charged particles in 2D cylindrical halo model of the Galaxy, the propagation of the antiprotons through the Galaxy is simulated. In these simulations $\bar{p}$ annihilation, energy losses, "tertiary production" and diffusive reacceleration are taken into account. The yellow uncertainty band of figure 19 shows the impact of the propagation onto the uncertainty. The MIN, MED and MAX lines show different sets of diffusion parameters that minimize or maximize the hypothetical primary, dark matter antiproton flux at Earth. Details of this transport simulation can be found in [79]. Finally antiprotons that want to reach Earth have to penetrate the heliosphere, where they are subject to Solar modulation. To reach Earth, the antiprotons have to work against the Solar magnetic field that shields the Earth from low energy particles. This causes the antiprotons to lose energy. The solar modulation makes that we are unsure about the size of this effect, which plays a bigger role for low energy particles than for high energy particles. The solar modulation is parameterized by the Fisk potential, ϕ_F. This effect is summarized in the green uncertainty band of figure 19.

4.2.2 Antiproton dark matter constraints

As said before figure 19 shows the predicted secondary $\bar{p}/p$ ratio, over plotted with the PAMELA [80] and AMS-02 [77] data. The fiducial curve assumes the reference values for the different contributions to the uncertainties. The coloured bands represent the different uncertainties as discussed in the section above. From figure 19 it is clear that there is no antiproton excess that can be identified with respect to the background, and thus there is no real need for primary sources. This also means that there is limited room left for a dark matter antiproton component.
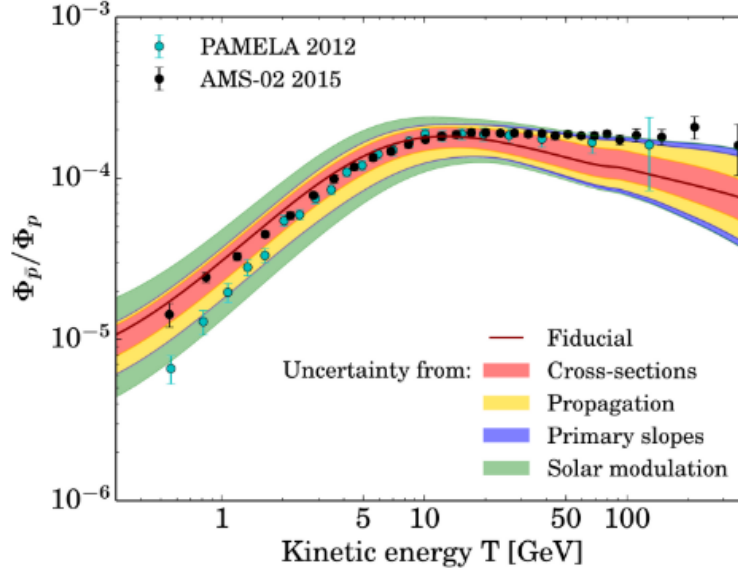

Figure 19: Figure from from [81] (partly based on figure 8 of [80]): The combined total uncertainty on the predicted secondary $\bar{p}/p$ ratio, superim-posed to the older Pamela data [78] and the new Ams-02 data [77]. The curve labelled 'fiducial' assumes the reference values for the different contributions to the uncertainties: best fit proton and helium fluxes, central values for the cross sections, Med propagation and central value for the Fisk potential. The colored bands represent the individual uncertainties on the input proton and helium fluxes (blue), $\bar{p}$ production cross sections in the interstellar medium (red), Galactic propagation (yellow) and Solar modulation (green).

To put constraints on the dark matter annihilation using the AMS-02 data following [81] four primary annihilation channels are considered: $\chi\chi \to b\bar{b}$, $\chi\chi \to W^+W^-$, $\chi\chi \to \mu^+\mu^-$ and $\chi\chi \to \gamma\gamma$. All of these products decay into antiprotons (and other particles). Using the recipe from [82] the maximum dark matter contributions to the antiproton - proton ratio are calculated for three different propagation models (MIN, MED and MAX). These are the sets of propagation parameters that minimize or maximize the a the dark matter antiproton flux at Earth. Fixing the propagation model to either of these, for a given dark matter mass and cross sections, the dark matter antiproton flux is added to the background: $\phi_{tot}(m_{DM}, <\sigma v>, A, \phi_F) = \phi_{background}(A, \phi_F) + \phi_{DM}(m_{DM}, <\sigma v>, \phi_F)$, where the best fit amplitude, A, and Fisk potential,ϕ_F, are implemented. By solving $\chi^2_{DM}(m_{DM}, <\sigma v>, A, \phi_F) - \chi^2_0 = 4$ (where χ_0 is the minimum chi-squared of the background-only case) for $<\sigma v>$ and thereby obtain an exclusion contour. This calculation is made for each dark matter mass. Also two dark matter density profiles, Einasto and Burkert, are considered. In the results of this calculation only the propagation schemes that provide a decent explanation of the background (MAX and MED) are taken into account.
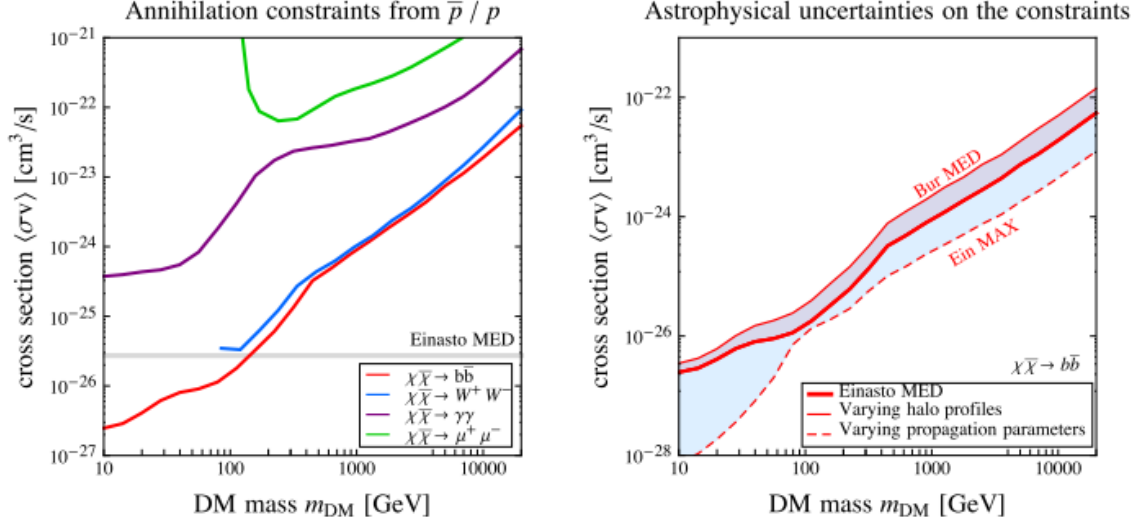
Figure 20: Figure from [81]: Annihilating dark matter: constraints based on AMS-02 data [77]. Left Panel: current constraints from the antiproton to proton ratio for different annihilation channels. The areas above the curves are excluded. Right Panel: illustration of the impact of dark matter-related astrophysical uncertainties: the constraint for the $\bar{b}b$ channel spans the shaded band when varying the propagation parameters (dashed lines) or the halo profiles (solid lines).

The resulting constraints on the cross section and mass are shown in figure 20. The left panels shows the constraints from the antiproton to proton ration for different annihilation channels but for fixed dark matter density profile (Einasto) and propagation parameters (MED). The areas above each of these lines are the cross section and mass regions that are excluded by these measurements. It is clear that the $\bar{b}b$ channel gives the strongest constraints, and the $\mu^+\mu^-$ channel the weakest. The latter is not surprising, since we don't expect much antiprotons from a leptonic channel. The right panel illustrates the impact of the astrophysical uncertainties for the $\bar{b}b$ channel. The dark matter density profile and propagation parameters give rise to the uncertainty band.

From the left panel of figure 20 it is clear that the limits on the cross section for the $b\bar{b}$ channel are the strongest and even exclude the thermal relic cross section at energies lower than ~ 100 GeV. The $\mu^+\mu^-$ and $\gamma\gamma$ channels are orders of magnitude weaker and don't provide very usefull con-
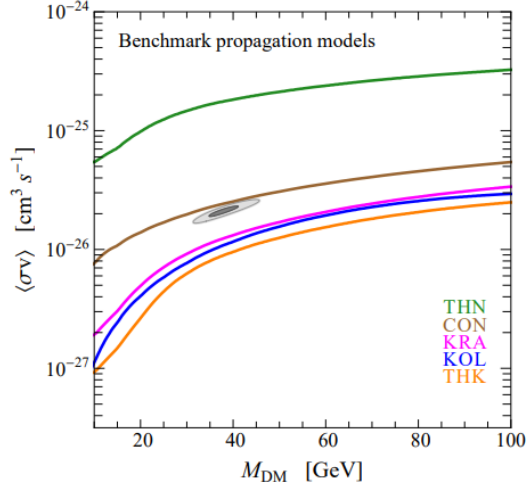

Figure 21: Figure from [83]: 3σ exclusion contours on $<\sigma v>$ for 100% dark matter annihilation into $b\bar{b}$. The Fick potential for the antiprotons is taken to be the Fick potential for protons: $\phi_F^{\bar{p}} = \phi_F^p \pm 50\%$. The different lines show different propagation set-ups. The gray area is the best-fit region identified for the claimed dark matter gamma-ray detection in [1].

straints. The right panel shows the difficulties in constraining the dark matter cross section via antiprotons, since the uncertainties in halo profile and propagation effects give rise to order of magnitude uncertainty bands.

Figure 21 show similar constraints to figure 20 using the antiproton fluxes from PAMELA [78] to explain the gamma-ray excess that was linked to dark matter by [1]. They show 3σ exclusion contours on $< \sigma v >$ for 100% dark matter annihilation into $b\bar{b}$. The Fick potential for the antiprotons is taken to be the Fick potential for protons: $\phi_F^{\bar{p}} = \phi_F^p \pm 50\%$. The different lines show different propagation set-ups. The thin propagation model (green) for example implies a thin dark matter halo. This means that antiprotons created in the galactic center are not able to scatter to Earth, therefore the observed flux is low and the constraints on the dark matter cross section weak. The thick propagation model (yellow) for example imposes a thick dark matter halo. This means that antiprotons created in the galactic center are able to scatter to Earth, therefore the observed flux is high and the constraints on the dark matter cross section are strong. The gray area is the best-fit region identified for the claimed dark matter gamma-ray detection in [1]. To find an agreement between the gamma-ray and antiproton data we have to exclude the THN and CON halo profile models. The other three halo models lie below the gray area and therefore it is possible that this claimed gamma-ray dark matter annihilation detection agrees with one of these models.

4.3   Anti-nucleus channel - (Paul)

A different approach of detecting dark matter would be to measure the flux of anti-nuclei, which consist of anti-nucleons that originate from dark matter annihilation processes. Specifically the anti-deuteron ($\bar{d}$) and anti-helium ($\overline{^3He}$) flux, which could give compelling hints towards dark matter. Although such signal has already been proposed over a decade ago, it has not been measured yet. Because of the high energy threshold of creating either one of the anti-nuclues, a large suppression is expected on the background signal at low kinetic energies, at the expense of having a extreme low flux signal. It is therefore important to simulate the expected flux that detectors have to measure on earth, in order to verify the dark matter in our Universe.

4.3.1   Anti-nuclei production

For the production of both the $\bar{d}$ and $\overline{^3He}$ nuclei, antiprotons and antineutrons need to coalesce. This process can be described by the coalescence model, see formula 19, which comes from relating the probability of finding a antineutron and antiproton within p_0 distance in momentum space, assuming equal neutron production cross sections and momentum distributions [84].

$$\gamma \frac{d^3 N_{\bar{A}}}{d\bar{p}_{\bar{A}}^3} = (\frac{4\pi}{3} p_0^3)^{(A-1)} (\gamma \frac{d^3 N_{\bar{p}}}{d\bar{p}_{\bar{p}}^3})^A \qquad (19)$$

Where A stands for the mass number of the nucleus, γ for the Lorentz factor and where the $\bar{p}$ spectrum has been normalized per annihilation event, see formula 20. The coalescence momentum p_0, is the effective momentum limit for which two nucleons will coalesce. This parameter, although extremely important for the spectrum, is unfortunately not well probed, moreover in section 4.3.2. Filling in $A = 2$ for $\bar{d}$ and $A = 3$ for $\overline{^3He}$, shows a dependence of $\propto p_0^3$ and $\propto p_0^6$ respectively, which is one of the major caveats of this method. It should also be noted that, as one would expect, increasing the mass number A will result in a suppression factor for the anti nuclei yield since typically $p_0 \sim O(0.1)$. We have therefore chosen to look at $\bar{d}$ and $\overline{^3He}$, increasing the mass number above this will result in a decrease in coalescence of a estimated factor $O(10^{-4})$, where knowledge on the $\bar{p}$ spectrum is
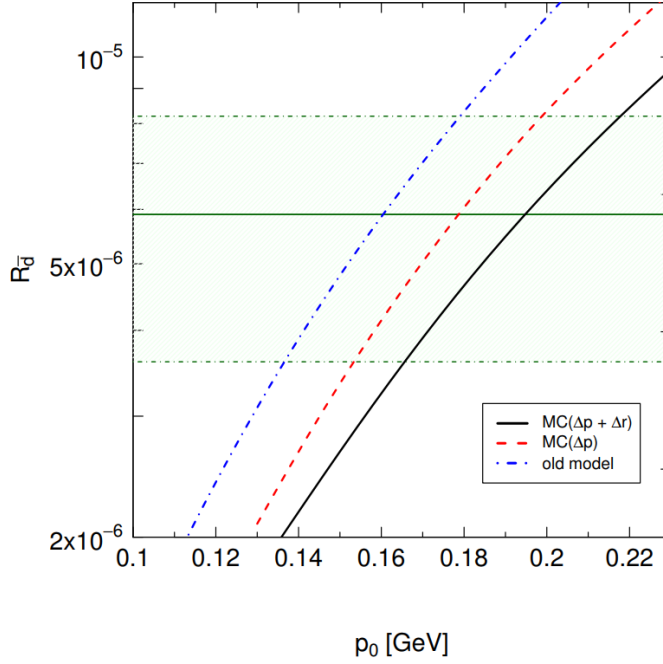
Figure 22: Figure from [86]: Production rate of anti-deuterons $\bar{d}$ from $e^+ + e^- \rightarrow \bar{d}$ at Z resonance as a function of coalescence momentum p_0 for three different models. The green line denotes the measurement by ALEPH.

assumed.

$$\frac{d^3 N_i}{d\vec{p}_i^3} = \frac{1}{\sigma_R} \frac{d^3 \sigma_i}{d\vec{p}_i^3} \tag{20}$$

Formula 20 shows the particle momentum spectrum, in which σ_R is the total nucleon-nucleus reaction cross section and where constrains on the cross section σ_i can be found in section 4.2.2.

4.3.2 Coalescence momentum p_0

As mentioned before, the momentum spectrum has a large dependence on coalescence momentum p_0. Since there is little experimental data taken for anti-nuclui, a similar production has been used to determine p_0, i.e. $e^+ + e^- \rightarrow \bar{d}$. Measurements by ALEPH on the $\bar{d}$ production rates trough said process have found to be $R_{\bar{d}} = (5.9 \pm 1.8 \pm 0.5) \times 10^{-6}$ anti-deuterons per Z-boson decay for momentum $\vec{p}_{\bar{d}} = (0.62, 1.03) GeV$, as shown in figure 22 (green line). Also depicted in this figure are three different models that calculate the production rate as a function of the coalescence momentum p_0:

- **Old Model**; in which uncorrelated production of $\bar{p}\bar{n}$ is assumed [85].

- **MC(Δp)**; Monte Carlo model in which the relative momentum of the $\bar{p}\bar{n}$ pair is cut off.

- **MC($\Delta p + \Delta r$)**; in which the previous model is extended to also include a cut off for the physical distance of the $\bar{p}\bar{n}$ pair.

Where it first should be noted that, determination of p_0 trough Z-boson decay does not resemble any particular dark matter candidate, but is rather done out of necessity since there is not much literature on this parameter. However, for light anti-nuclui (i.e. $A \leq 4$), consistent results have been found in case of astrophysical spallations between $\bar{d}$ and $^3\overline{He}$ while using the same coalescence momentum p_0. Secondly, it is assumed that the coalescence momentum p_0 is constant. Imagining a energy dependence on this parameter would change the anti-nuclei spectrum drastically, but since this is not tested, the assumption could be valid. Looking at the measurement by ALEPH $R_{\bar{d}} = (5.9 \pm 1.8 \pm 0.5) \times 10^{-6}$, we find the following 1σ significance results to be: **Old Model** $\rightarrow p_0 = 160 \pm 19 MeV$, **MC($\Delta p$)** $\rightarrow p_0 = 180 \pm 18 MeV$ and **MC($\Delta p + \Delta r$)** $\rightarrow p_0 = 195 \pm 22 MeV$. Because the coalescence spectrum heavily depends on this value (i.e. to the power $3 - 6$, see section 4.3.1), the differences between model results become quite large, especially when looking at the uncertainties that are about ten percent. Continuing our $\bar{d}$ and $^3\overline{He}$ flux simulation, we will use the coalescence momentum value of $p_0 = 195 MeV$ [86].

4.3.3   Propagation

After anti-nuclei have been produced, they propagate trough the galactic medium towards a detector on earth. Their number density $f(t, \vec{x}, T) = dN_{\bar{d}, \overline{He}}/dT$ per unit of kinetic energy T can then be described by formula 21, for which we closely follow [87] and [86].

$$\frac{\partial f}{\partial t} - K(T) \cdot \Lambda^2 f + \frac{\partial}{\partial z}(sign(z)fV_c) = Q - 2h\delta(z)\nabla f \tag{21}$$

In which $K(T)$ is a diffusion coefficient via a two-zone diffusion model in which cosmic rays interact with the inter stellar medium (ISM), V_c is a convective velocity of galactic wind, Q the dark matter annihilation source term, which we have seen before in equation 1 for different dark matter density profiles, but now with a anti-nuclei spectrum. The last term includes: ∇ the annihilation rate of $\bar{d}$ (due to ISM interactions), $\delta(z)$ refers to the galactic plane and h to its height.
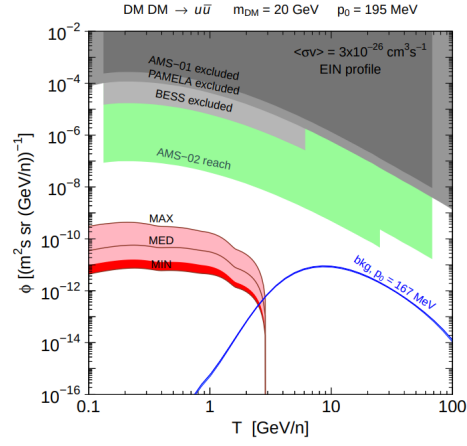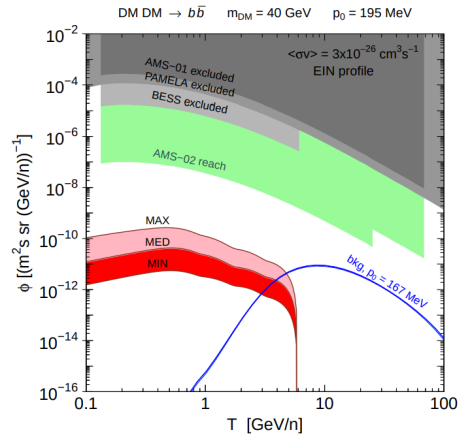
Figure 23: Figure from [87]:

Figure 24: Figure from [87]:

4.3.4 Results

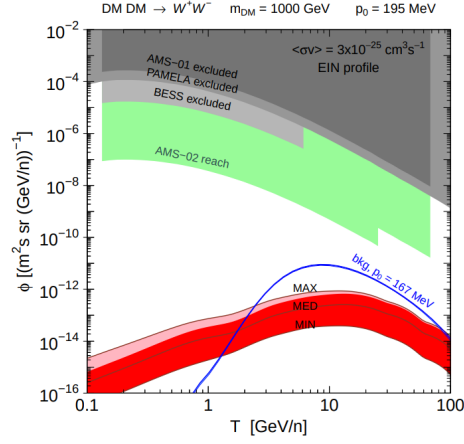Conclusie: Ams-02 gaat het niet redden voor He.

Figure 25: Figure from [87]:

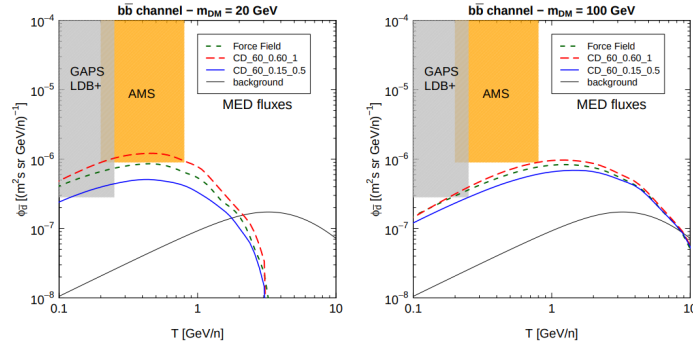|	Galactic charged CR propagation parameters			
Model	δ	$\mathcal{K}_0$ [kpc^2/Myr]	V_{conv} [km/s]	L [kpc]
MIN	0.85	0.0016	13.5	1
MED	0.70	0.0112	12	4
MAX	0.46	0.0765	5	15

Figure 26: Table from [87]:
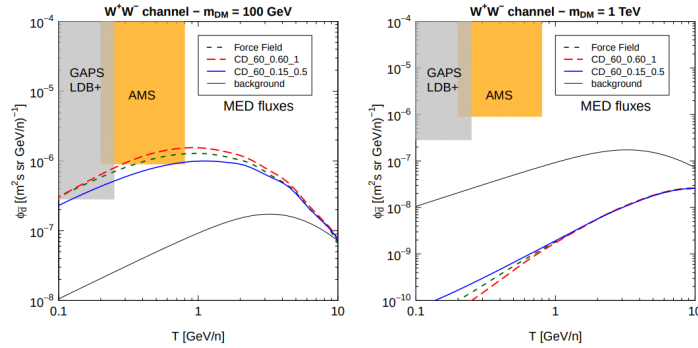

Figure 27: Figure from [87]:

Figure 28: Figure from [87]:

5 Code

The Jupyter notebook named J_factors.ipynb can be used to experiment with and calculate the J-factors of different dwarf galaxies and galaxy clusters. The calculation of the J-factors is described in section 2.1 in equation 4. The input parameters are described in the code and can be used to plot the J-factor and/or D-factor of the Milky Way, blabla clusters. If there was any observational data available, this is overplotted.

5.1 Data

The J-factor data for the dwarf galaxies is taken from [88], the Milky way data is from [89]. To calculate the scale radii we used 5 times the half-radii as described in [90]. The central density for the dwarf galaxies was calculated using the relation between central density and scale radius as described by Burkert: [91]

$$\rho_0 = 2.7 \cdot 10^{-2} \left(\frac{r_s}{kpc} \right)^{-2/3} \frac{M_\odot}{pc^3} \tag{22}$$

This density was afterwards converted to the right units (GeV/cm^3).
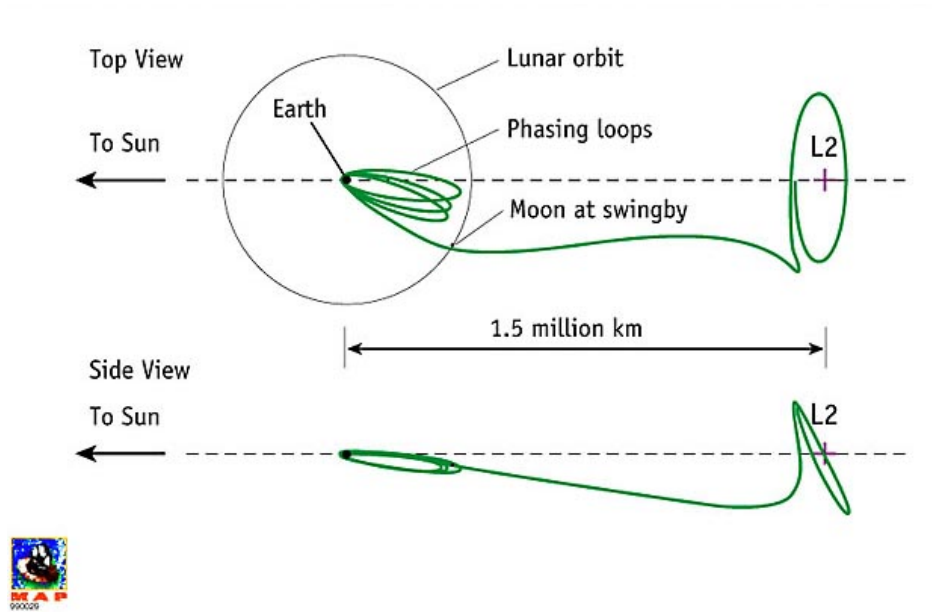
6 Appendix

6.1 Appendix A

Figure 29: Figure from NASA website. WMAP lunar assisted trajectory to the Sun-Earth L2 libration point.

References

[1] Tansu Daylan, Douglas P Finkbeiner, Dan Hooper, Tim Linden, Stephen KN Portillo, Nicholas L Rodd, and Tracy R Slatyer. The characterization of the gamma-ray signal from the central milky way: A case for annihilating dark matter. *Physics of the Dark Universe*, 12:1–23, 2016.

[2] Richard Bartels, Suraj Krishnamurthy, and Christoph Weniger. Strong support for the millisecond pulsar origin of the galactic center gev excess. *Physical Review Letters*, 116(5):051102, 2016.

[3] T. M. Nieuwenhuizen. Subjecting dark matter candidates to the cluster test. *ArXiv e-prints*, October 2017.

[4] A. Bottino, V. de Alfaro, N. Fornengo, G. Mignola, and S. Scopel. On the neutralino as dark matter candidate. II. Direct detection. *Astroparticle Physics*, 2:77–90, February 1994.

[5] Jennifer M. Gaskins. A review of indirect searches for particle dark matter. *Contemporary Physics*, 57(4):496–525, 2016.

[6] Marco Cirelli, Gennaro Corcella, Andi Hektor, Gert Hütsi, Mario Kadastik, Paolo Panci, Martti Raidal, Filippo Sala, and Alessandro Strumia. Pppc 4 dm id: a poor particle physicist cookbook for dark matter indirect detection. *Journal of Cosmology and Astroparticle Physics*, 2011(03):051, 2011.

[7] A. Abramowski, F. Aharonian, F. Ait Benkhali, A. G. Akhperjanian, E. Angüner, M. Backes, S. Balenderan, A. Balzer, A. Barnacka, Y. Becherini, and et al. Search for dark matter annihilation signatures in H.E.S.S. observations of dwarf spheroidal galaxies. *Physical Review*, 90(11):112012, December 2014.

[8] Fabio Iocco, Miguel Pato, Gianfranco Bertone, and Philippe Jetzer. Dark matter distribution in the milky way: microlensing and dynamical constraints. *Journal of Cosmology and Astroparticle Physics*, 2011(11):029, 2011.

[9] Frank C. van den Bosch and Rob A. Swaters. Dwarf galaxy rotation curves and the core problem of dark matter haloes. *Monthly Notices of the Royal Astronomical Society*, 325(3):1017–1038, 2001.

[10] J. Diemand, M. Kuhlen, P. Madau, M. Zemp, B. Moore, D. Potter, and J. Stadel. Clumps and streams in the local dark matter distribution. *Nature*, 454:735–738, August 2008.

[11] Mattia Fornasa and Anne M Green. Self-consistent phase-space distribution function for the anisotropic dark matter halo of the milky way. *Physical Review D*, 89(6):063531, 2014.

[12] Paolo Gondolo and Joseph Silk. Dark matter annihilation at the galactic center. *Physical Review Letters*, 83(9):1719, 1999.

[13] Oleg Y Gnedin, Andrey V Kravtsov, Anatoly A Klypin, and Daisuke Nagai. Response of dark matter halos to condensation of baryons: cosmological simulations and improved adiabatic contraction model. *The Astrophysical Journal*, 616(1):16, 2004.

[14] Oleg Y Gnedin, Daniel Ceverino, Nickolay Y Gnedin, Anatoly A Klypin, Andrey V Kravtsov, Robyn Levine, Daisuke Nagai, and Gustavo Yepes. Halo contraction effect in hydrodynamic simulations of galaxy formation. *arXiv preprint arXiv:1108.5736*, 2011.

[15] B. Moore, T. Quinn, F. Governato, J. Stadel, and G. Lake. Cold collapse and the core catastrophe. *Monthly Notices of the Royal Astronomical Society*, 310:1147–1152, December 1999.

[16] J. J. Adams, J. D. Simon, M. H. Fabricius, R. C. E. van den Bosch, J. C. Barentine, R. Bender, K. Gebhardt, G. J. Hill, J. D. Murphy, R. A. Swaters, J. Thomas, and G. van de Ven. Dwarf Galaxy Dark Matter Density Profiles Inferred from Stellar and Gas Kinematics. *The astrophysical journal*, 789:63, July 2014.

[17] J. F. Navarro, E. Hayashi, C. Power, A. R. Jenkins, C. S. Frenk, S. D. M. White, V. Springel, J. Stadel, and T. R. Quinn. The inner structure of ΛCDM haloes - III. Universality and asymptotic slopes. *Monthly Notices of the Royal Astronomical Society*, 349:1039–1051, April 2004.

[18] Liang Gao, Julio F Navarro, Shaun Cole, Carlos S Frenk, Simon DM White, Volker Springel, Adrian Jenkins, and Angelo F Neto. The redshift dependence of the structure of massive λ cold dark matter haloes. *Monthly Notices of the Royal Astronomical Society*, 387(2):536–544, 2008.

[19] J. F. Navarro, A. Ludlow, V. Springel, J. Wang, M. Vogelsberger, S. D. M. White, A. Jenkins, C. S. Frenk, and A. Helmi. The diversity and similarity of simulated cold dark matter haloes. *Monthly Notices of the Royal Astronomical Society*, 402:21–34, February 2010.

[20] J. Einasto. On the Construction of a Composite Model for the Galaxy and on the Determination of the System of Galactic Parameters. *Trudy Astrofizicheskogo Instituta Alma-Ata*, 5:87–100, 1965.

[21] Gianfranco Bertone, Andrew R Zentner, and Joseph Silk. New signature of dark matter annihilations: Gamma rays from intermediate-mass black holes. *Physical Review D*, 72(10):103517, 2005.

[22] WB Atwood, Aous A Abdo, Markus Ackermann, W Althouse, B Anderson, M Axelsson, L Baldini, J Ballet, DL Band, Guido Barbiellini, et al. The large area telescope on the fermi gamma-ray space telescope mission. *The Astrophysical Journal*, 697(2):1071, 2009.

[23] Markus Ackermann, Marco Ajello, WB Atwood, Luca Baldini, Guido Barbiellini, D Bastieri, K Bechtol, R Bellazzini, RD Blandford, ED Bloom, et al. Constraints on the galactic halo dark matter from fermi-lat diffuse measurements. *The Astrophysical Journal*, 761(2):91, 2012.

[24] Andrea Albert, Brandon Anderson, Keith Bechtol, Alex Drlica-Wagner, Manuel Meyer, Miguel Sánchez-Conde, L Strigari, M Wood, TMC Abbott, Filipe B Abdalla, et al. Searching for dark matter annihilation in recently discovered milky way satellites with fermi-lat. *The Astrophysical Journal*, 834(2):110, 2017.

[25] M Ackermann, A Albert, Brandon Anderson, WB Atwood, L Baldini, G Barbiellini, D Bastieri, K Bechtol, R Bellazzini, E Bissaldi, et al. Searching for dark matter annihilation from milky way dwarf spheroidal galaxies with six years of fermi large area telescope data. *Physical Review Letters*, 115(23):231301, 2015.

[26] Gary Steigman, Basudeb Dasgupta, and John F Beacom. Precise relic wimp abundance and its impact on searches for dark matter annihilation. *Physical Review D*, 86(2):023506, 2012.

[27] Felix Aharonian, AG Akhperjanian, AR Bazer-Bachi, M Beilicke, Wystan Benbow, David Berge, K Bernlöhr, C Boisson, Oliver Bolz, V Borrel, et al. Hess observations of the galactic center region and their possible dark matter interpretation. *Physical Review Letters*, 97(22):221102, 2006.

[28] A Abramowski, Fabio Acero, F Aharonian, AG Akhperjanian, G Anton, A Barnacka, U Barres De Almeida, AR Bazer-Bachi, Yvonne Becherini, J Becker, et al. Search for a dark matter annihilation signal from the galactic center halo with hess. *Physical Review Letters*, 106(16):161301, 2011.

[29] H. Abdallah et al. Search for γ-Ray Line Signals from Dark Matter Annihilations in the Inner Galactic Halo from 10 Years of Observations with H.E.S.S. *Phys. Rev. Lett.*, 120(20):201101, 2018.

[30] S Archambault, A Archer, W Benbow, R Bird, E Bourbeau, T Brantseg, M Buchovecky, JH Buckley, V Bugaev, K Byrum, et al. Dark matter constraints from a joint analysis of dwarf spheroidal galaxy observations with veritas. *Physical Review D*, 95(8):082001, 2017.

[31] Max L Ahnen, S Ansoldi, LA Antonelli, C Arcaro, D Baack, A Babić, B Banerjee, P Bangale, U Barres de Almeida, JA Barrio, et al. Indirect dark matter searches in the dwarf satellite galaxy ursa major ii with the magic telescopes. *Journal of Cosmology and Astroparticle Physics*, 2018(03):009, 2018.

[32] AU Abeysekara, A Albert, R Alfaro, C Alvarez, R Arceo, JC Arteaga-Velázquez, D Avila Rojas, HA Ayala Solares, A Becerril, E Belmont-Moreno, et al. A search for dark matter in the galactic halo with hawc. *Journal of Cosmology and Astroparticle Physics*, 2018(02):049, 2018.

[33] The Cherenkov Telescope Array Consortium, BS Acharya, I Agudo, I Al Samarai, R Alfaro, J Alfaro, C Alispach, R Alves Batista, J-P Amans, E Amato, et al. Science with the cherenkov telescope array. *arXiv preprint arXiv:1709.07997*, 2017.

[34] The CTA Consortium. Design concepts for the cherenkov telescope array. *arXiv preprint arXiv:1008.3703*, 2010.

[35] Hamish Silverwood, Christoph Weniger, Pat Scott, and Gianfranco Bertone. A realistic assessment of the cta sensitivity to dark matter annihilation. *Journal of Cosmology and Astroparticle Physics*, 2015(03):055, 2015.

[36] O Adriani, Y Akaike, K Asano, Y Asaoka, MG Bagliesi, G Bigongiari, WR Binns, S Bonechi, M Bongi, JH Buckley, et al. The calorimetric electron telescope (calet) for high-energy astroparticle physics on the international space station. In *Journal of Physics: Conference Series*, volume 632, page 012023. IOP Publishing, 2015.

[37] NP Topchiev, AM Galper, V Bonvicini, O Adriani, RL Aptekar, IV Arkhangelskaja, AI Arkhangelskiy, AV Bakaldin, L Bergstrom, E Berti, et al. Gamma-400 gamma-ray observatory. *arXiv preprint arXiv:1507.06246*, 2015.

[38] Xiaoyuan Huang, Anna S Lamperstorfer, Yue-Lin Sming Tsai, Ming Xu, Qiang Yuan, Jin Chang, Yong-Wei Dong, Bing-Liang Hu, Jun-Guang Lü, Le Wang, et al. Perspective of monochromatic gamma-ray line detection with the high energy cosmic-radiation detection (herd) facility onboard china's space station. *Astroparticle Physics*, 78:35–42, 2016.

[39] Silvia Galli, Fabio Iocco, Gianfranco Bertone, and Alessandro Melchiorri. Cmb constraints on dark matter models with large annihilation cross section. *Physical Review D*, 80(2):023505, 2009.

[40] Antony Lewis, Jochen Weller, and Richard Battye. The cosmic microwave background and the ionization history of the universe. *Monthly Notices of the Royal Astronomical Society*, 373(2):561–570, 2006.

[41] Silvia Galli, Rachel Bean, Alessandro Melchiorri, and Joseph Silk. Delayed recombination and cosmic parameters. *Phys. Rev. D*, 78:063532, Sep 2008.

[42] Jaiseung Kim and Pavel Naselsky. Accelerated recombination, and the acbar and wmap data. *The Astrophysical Journal Letters*, 678(1):L1, 2008.

[43] N Aghanim, M Arnaud, M Ashdown, J Aumont, C Baccigalupi, AJ Banday, RB Barreiro, JG Bartlett, N Bartolo, E Battaner, et al. Planck 2015 results-xi. cmb power spectra, likelihoods, and robustness of parameters. *Astronomy & Astrophysics*, 594:A11, 2016.

[44] Le Zhang, Xuelei Chen, Yi-An Lei, and Zong-guo Si. Impacts of dark matter particle annihilation on recombination and the anisotropies of the cosmic microwave background. *Physical Review D*, 74(10):103519, 2006.

[45] A Lewis, A Challinor, and A Lasenby. Efficient computation of cmb anisotropies in closed frw models. *Astrophys. J*, 538:473, 2000.

[46] Sara Seager, Dimitar D Sasselov, and Douglas Scott. How exactly did the universe become neutral? *The Astrophysical Journal Supplement Series*, 128(2):407, 2000.

[47] PJE Peebles. Recombination of the primeval plasma. *The Astrophysical Journal*, 153:1, 1968.

[48] Nikhil Padmanabhan and Douglas P Finkbeiner. Detecting dark matter annihilation with cmb polarization: Signatures and experimental prospects. *Physical Review D*, 72(2):023508, 2005.

[49] O Adriani, GC Barbarino, GA Bazilevskaya, R Bellotti, M Boezio, EA Bogomolov, L Bonechi, M Bongi, V Bonvicini, S Bottai, et al. Observation of an anomalous positron abundance in the cosmic radiation. *arXiv preprint arXiv:0810.4995*, 2008.

[50] Ilias Cholis, Douglas P Finkbeiner, Lisa Goodenough, and Neal Weiner. The pamela positron excess from annihilations into a light boson. *Journal of Cosmology and Astroparticle Physics*, 2009(12):007, 2009.

[51] Massimiliano Lattanzi and Joseph Silk. Can the wimp annihilation boost factor be boosted by the sommerfeld enhancement? *Physical Review D*, 79(8):083523, 2009.

[52] Jesus Zavala, Mark Vogelsberger, and Simon DM White. Relic density and cmb constraints on dark matter annihilation with sommerfeld enhancement. *Physical Review D*, 81(8):083502, 2010.

[53] Tracy R. Slatyer. Indirect dark matter signatures in the cosmic dark ages. I. Generalizing the bound on s -wave dark matter annihilation from Planck results. *Physical Review D*, 93(2):023527, jan 2016.

[54] Mathew S. Madhavacheril, Neelima Sehgal, and Tracy R. Slatyer. Current dark matter annihilation constraints from CMB and low-redshift data. *Physical Review D*, 89(10):103508, may 2014.

[55] Sara Seager, Dimitar D. Sasselov, and Douglas Scott. RECFAST: Calculate the Recombination History of the Universe. *Astrophysics Source Code Library, record ascl:1106.026*, 2011.

[56] G. Hütsi, J. Chluba, A. Hektor, and M. Raidal. WMAP7 and future CMB constraints on annihilating dark matter: implications for GeV-scale WIMPs. *Astronomy & Astrophysics*, 535:A26, nov 2011.

[57] D Larson, J Dunkley, G Hinshaw, Eiichiro Komatsu, MR Nolta, CL Bennett, B Gold, M Halpern, RS Hill, N Jarosik, et al. Seven-year wilkinson microwave anisotropy probe (wmap*) observations: power spectra and wmap-derived parameters. *The Astrophysical Journal Supplement Series*, 192(2):16, 2011.

[58] DJ Eisenstein et al. Detection of the baryon acoustic peak in the large-scale correlation function of sdss luminous red galaxies. *Astrophys. J*, 633:560, 2005.

[59] Laura Lopez-Honorez, Olga Mena, Sergio Palomares-Ruiz, and Aaron C Vincent. Constraints on dark matter annihilation from CMB observations before Planck. *Journal of Cosmology and Astroparticle Physics*, 2013(07):046–046, jul 2013.

[60] E. Komatsu, J. Dunkley, M. R. Nolta, C. L. Bennett, B. Gold, G. Hinshaw, N. Jarosik, D. Larson, M. Limon, L. Page, D. N. Spergel, M. Halpern, R. S. Hill, A. Kogut, S. S. Meyer, G. S. Tucker, J. L. Weiland, E. Wollack, and E. L. Wright. Five-Year Wilkinson Microwave Anisotropy Probe Observations: Cosmological Interpretation. *The astrophysical journal*, 180:330–376, February 2009.

[61] NASA. https://wmap.gsfc.nasa.gov/. 2001.

[62] Pasquale Dario Serpico and Pasquale D. Possible causes of a rise with energy of the cosmic ray positron fraction. *Physical Review D, vol. 79, Issue 2, id. 021302*, 79(2), oct 2008.

[63] Pasquale D. Serpico. Astrophysical models for the origin of the positron "excess". *Astroparticle Physics*, 39-40:2–11, dec 2012.

[64] Oscar Adriani, GC Barbarino, GA Bazilevskaya, R Bellotti, Mirko Boezio, EA Bogomolov, L Bonechi, M Bongi, Valter Bonvicini, S Bottai, et al. An anomalous positron abundance in cosmic rays with energies 1.5–100 gev. *Nature*, 458(7238):607, 2009.

[65] O Adriani, GC Barbarino, GA Bazilevskaya, R Bellotti, M Boezio, EA Bogomolov, L Bonechi, M Bongi, V Bonvicini, S Borisov, et al. A statistical procedure for the identification of positrons in the pamela experiment. *Astroparticle Physics*, 34(1):1–11, 2010.

[66] Giuseppe Di Bernardo, Carmelo Evoli, Daniele Gaggero, Dario Grasso, and Luca Maccione. Unified interpretation of cosmic ray nuclei and antiproton recent measurements. *Astroparticle Physics*, 34(5):274–283, dec 2010.

[67] J. Lavalle. Impact of the spectral hardening of TeV cosmic rays on the prediction of the secondary positron flux. *Monthly Notices of the Royal Astronomical Society*, 414(2):985–991, jun 2011.

[68] I. V. Moskalenko and A. W. Strong. Production and Propagation of Cosmic-Ray Positrons and Electrons. *The Astrophysical Journal*, 493(2):694–707, feb 1998.

[69] Nir J. Shaviv, Ehud Nakar, and Tsvi Piran. Inhomogeneity in the Supernova Remnant Distribution as the Origin of the PAMELA Anomaly. *Physical Review Letters*, 103(11):111302, feb 2009.

[70] James Stockton. Average inhomogeneities in Milky Way SNII and the PAMELA anomaly. *Astroparticle Physics*, 35(3):161–163, oct 2011.

[71] Markus Ackermann, Marco Ajello, A Allafort, WB Atwood, Luca Baldini, Guido Barbiellini, D Bastieri, K Bechtol, R Bellazzini, B Berenji, et al. Measurement of separate cosmic-ray electron and positron spectra with the fermi large area telescope. *Physical Review Letters*, 108(1):011103, 2012.

[72] Dan Hooper, Albert Stebbins, and Kathryn M. Zurek. Excesses in cosmic ray positron and electron spectra from a nearby clump of neutralino dark matter. *Physical Review D*, 79(10):103513, may 2009.

[73] Stuart L. Shapiro and Saul A. Teukolsky. Black holes, white dwarfs, and neutron stars: The physics of compact objects. *Research supported by the National Science Foundation. New York, Wiley-Interscience, 1983, 663 p.*, 1983.

[74] John Ellis, RA Flores, Katherine Freese, S Ritz, D Seckel, and Joseph Silk. Cosmic ray constraints on the annihilations of relic particles in the galactic halo. *Physics Letters B*, 214(3):403–412, 1988.

[75] Pasquale D Serpico. Astrophysical models for the origin of the positron "excess". *Astroparticle Physics*, 39:2–11, 2012.

[76] F Donato, D Maurin, P Brun, T Delahaye, and P Salati. Constraints on wimp dark matter from the high energy pamela p̄/p data. *Physical review letters*, 102(7):071301, 2009.

[77] M Aguilar, L Ali Cavasonza, B Alpat, G Ambrosi, L Arruda, N Attig, S Aupetit, P Azzarello, A Bachlechner, F Barao, et al. Antiproton flux, antiproton-to-proton flux ratio, and properties of elementary particle fluxes in primary cosmic rays measured with the alpha magnetic spectrometer on the international space station. *Physical review letters*, 117(9):091103, 2016.

[78] O Adriani, GC Barbarino, GA Bazilevskaya, R Bellotti, M Boezio, EA Bogomolov, L Bonechi, M Bongi, V Bonvicini, S Borisov, et al. Pamela measurements of cosmic-ray proton and helium spectra. *arXiv preprint arXiv:1103.4055*, 2011.

[79] Mathieu Boudaud, Marco Cirelli, Gaëlle Giesen, and Pierre Salati. A fussy revisitation of antiprotons as a tool for dark matter searches. *Journal of Cosmology and Astroparticle Physics*, 2015(05):013, 2015.

[80] Mattia Di Mauro, Fiorenza Donato, Andreas Goudelis, and Pasquale Dario Serpico. New evaluation of the antiproton production cross section for cosmic ray studies. *Physical Review D*, 90(8):085017, 2014.

[81] Gaëlle Giesen, Mathieu Boudaud, Yoann Genolini, Vivian Poulin, Marco Cirelli, Pierre Salati, and Pasquale D Serpico. Ams-02 antiprotons, at last! secondary astrophysical component and immediate implications for dark matter. *Journal of Cosmology and Astroparticle Physics*, 2015(09):023, 2015.

[82] Marco Cirelli, Gennaro Corcella, Andi Hektor, Gert Hütsi, Mario Kadastik, Paolo Panci, Martti Raidal, Filippo Sala, and Alessandro Strumia. Pppc 4 dm id: a poor particle physicist cookbook for dark matter indirect detection. *Journal of Cosmology and Astroparticle Physics*, 2011(03):051, 2011.

[83] Marco Cirelli, Daniele Gaggero, Gaëlle Giesen, Marco Taoso, and Alfredo Urbano. Antiproton constraints on the gev gamma-ray excess: a comprehensive analysis. *Journal of Cosmology and Astroparticle Physics*, 2014(12):045, 2014.

[84] R. Duperray, B. Baret, D. Maurin, G. Boudoul, A. Barrau, L. Derome, K. Protasov, and M. Buénerd. Flux of light antimatter nuclei near Earth, induced by cosmic rays in the Galaxy and in the atmosphere. *Physical Review*, 71(8):083013, April 2005.

[85] F. Donato, N. Fornengo, and P. Salati. Antideuterons as a signature of supersymmetric dark matter. *Physical Review*, 62(4):043003, August 2000.

[86] N. Fornengo, L. Maccione, and A. Vittino. Dark matter searches with cosmic antideuterons: status and perspectives. *Journal of Cosmology and Astroparticle Physics*, 9:031, September 2013.

[87] M. Cirelli, N. Fornengo, M. Taoso, and A. Vittino. Anti-helium from dark matter annihilations. *Journal of High Energy Physics*, 8:9, August 2014.

[88] NW Evans, JL Sanders, and Alex Geringer-Sameth. Simple j-factors and d-factors for indirect dark matter detection. *Physical Review D*, 93(10):103512, 2016.

[89] A Albert, Michel André, Marco Anghinolfi, G Anton, M Ardid, J-J Aubert, T Avgitas, B Baret, J Barrios-Martí, S Basa, et al. Results from the search for dark matter in the milky way with 9 years of data of the antares neutrino telescope. *Physics letters B*, 769:249–254, 2017.

[90] Alex Geringer-Sameth, Savvas M Koushiappas, and Matthew Walker. Dwarf galaxy annihilation and decay emission profiles for dark matter experiments. *The Astrophysical Journal*, 801(2):74, 2015.

[91] Andreas Burkert. The structure of dark matter halos in dwarf galaxies. *The Astrophysical Journal Letters*, 447(1):L25, 1995.

6.2 Review papers

https://arxiv.org/pdf/1707.06277.pdf WIMP dark matter candidates and searches – current status and future prospects

Indirect detection of dark matter - Lars Bergstrom (2007)

J. M. Gaskins, A review of indirect searches for particle dark matter, Contemp. Phys. (2016) https://arxiv.org/pdf/1604.00014.pdf

Indirect detection of dark matter - J. Carr et al. (2006)

Ackerman et al. (2015) ; "*Searching for Dark Matter Annihilation from Milky Way Dwarf Spheroidal Galaxies with Six Years of Fermi Large Area Telescope Data*"

6.3 Scale Radii

M. A. Breddels and A. Helmi, "Model comparison of the dark matter profiles of Fornax, Sculptor, Carina and Sextans", A&A 559, 10 p., (2013) https://arxiv.org/pdf/1304.2976.pdf

6.4 ID DM signal radiative transfer

Profumo, S. and Jeltema, E.T. (2011) ; "*Extragalactic Inverse Compton Light from Dark Matter annihilation and the Pamela positron excess*" http://iopscience.iop.org/article/10.1088/1475-7516/2009/07/020/meta